AGU PUBLICATIONS

JGR

Journal of Geophysical Research: Space Physics

RESEARCH ARTICLE
10.1002/2015JA021454

Key Points:
- We study Saturn's preequinox northern auroral field-aligned currents (FACs)
- FACs modulated equally by north and south planetary period oscillations (PPOs)
- Data provide first direct evidence of interhemispheric PPO-related FAC

Correspondence to:
G. J. Hunt,
gjh19@le.ac.uk

Citation:
Hunt, G. J., S. W. H. Cowley, G. Provan, E. J. Bunce, I. I. Alexeev, E. S. Belenkaya, V. V. Kalegaev, M. K. Dougherty, and A. J. Coates (2015), Field-aligned currents in Saturn's northern nightside magnetosphere: Evidence for interhemispheric current flow associated with planetary period oscillations, *J. Geophys. Res. Space Physics*, *120*, 7552–7584, doi:10.1002/2015JA021454.

Received 11 MAY 2015
Accepted 23 AUG 2015
Accepted article online 26 AUG 2015
Published online 26 SEP 2015

Field-aligned currents in Saturn's northern nightside magnetosphere: Evidence for interhemispheric current flow associated with planetary period oscillations

G. J. Hunt[1], S. W. H. Cowley[1], G. Provan[1], E. J. Bunce[1], I. I. Alexeev[2], E. S. Belenkaya[2], V. V. Kalegaev[2], M. K. Dougherty[3], and A. J. Coates[4]

[1]Department of Physics and Astronomy, University of Leicester, Leicester, UK, [2]Skobeltsyn Institute of Nuclear Physics, Lomonosov Moscow State University, Moscow, Russia, [3]Blackett Laboratory, Imperial College London, London, UK, [4]Mullard Space Science Laboratory, University College London, Dorking, UK

Abstract We investigate the magnetic perturbations associated with field-aligned currents observed on 34 Cassini passes over the premidnight northern auroral region during 2008. These are found to be significantly modulated not only by the northern planetary-period oscillation (PPO) system, similar to the southern currents by the southern PPO system found previously, but also by the southern PPO system as well, thus providing the first clear evidence of PPO-related interhemispheric current flow. The principal field-aligned currents of the two PPO systems are found to be co-located in northern ionospheric colatitude, together with the currents of the PPO-independent (subcorotation) system, located between the vicinity of the open-closed field boundary and field lines mapping to ~9 Saturn radius (R_S) in the equatorial plane. All three systems are of comparable magnitude, ~3 MA in each PPO half-cycle. Smaller PPO-related field-aligned currents of opposite polarity also flow in the interior region, mapping between ~6 and ~9 R_S in the equatorial plane, carrying a current of ~ ±2 MA per half-cycle, which significantly reduce the oscillation amplitudes in the interior region. Within this interior region the amplitudes of the northern and southern oscillations are found to fall continuously with distance along the field lines from the corresponding hemisphere, thus showing the presence of cross-field currents, with the southern oscillations being dominant in the south, and modestly lower in amplitude than the northern oscillations in the north. As in previous studies, no oscillations related to the opposite hemisphere are found on open field lines in either hemisphere.

1. Introduction

The means by which momentum is communicated between a planetary atmosphere and the plasma environment beyond is fundamental to the physics of such systems. Electric currents flowing transverse to the magnetic field in both the planetary ionosphere and the magnetosphere imply the presence of $\boldsymbol{j} \times \boldsymbol{B}$ forces on these plasma mediums, the transverse currents being linked by currents flowing along the planetary magnetic field lines between them to form large-scale closed-loop current systems. In the case of Saturn, the primary focus of the present paper, the principal current systems are those related to subcorotation of the magnetospheric plasma [e.g., *Cowley and Bunce*, 2003; *Wilson et al*., 2009; *Pontius and Hill*, 2009; *Thomsen et al*., 2014] and to the "planetary period oscillations" (PPOs) whose effects have been found to be ubiquitous in Saturn's magnetosphere [e.g., *Carbary and Mitchell*, 2013, and references therein]. In a recent paper *Hunt et al*. [2014] examined the magnetic field perturbations observed on a sequence of ~40 periapsis passes of the Cassini spacecraft over Saturn's nightside auroral regions in 2008 and separated the effects of these two current systems using their opposite symmetry properties. However, that paper examined only the data from the passes over the southern auroral region, such that here we complete the survey by also examining the northern data. We note that other variable current systems may also generally be present associated with the solar wind interaction [e.g., *Cowley et al*., 2004a; *Southwood and Kivelson*, 2009; *Radioti et al*., 2013; *Meredith et al*., 2013, 2014], fixed in local time (LT) principally on the dayside, but since the observations to be discussed here are restricted to a narrow LT sector on the nightside, these will not be considered further here.

The expected forms of the above current systems are sketched for future reference in Figure 1. In these diagrams the black arrowed lines show the background magnetic field lines, the green arrowed lines and

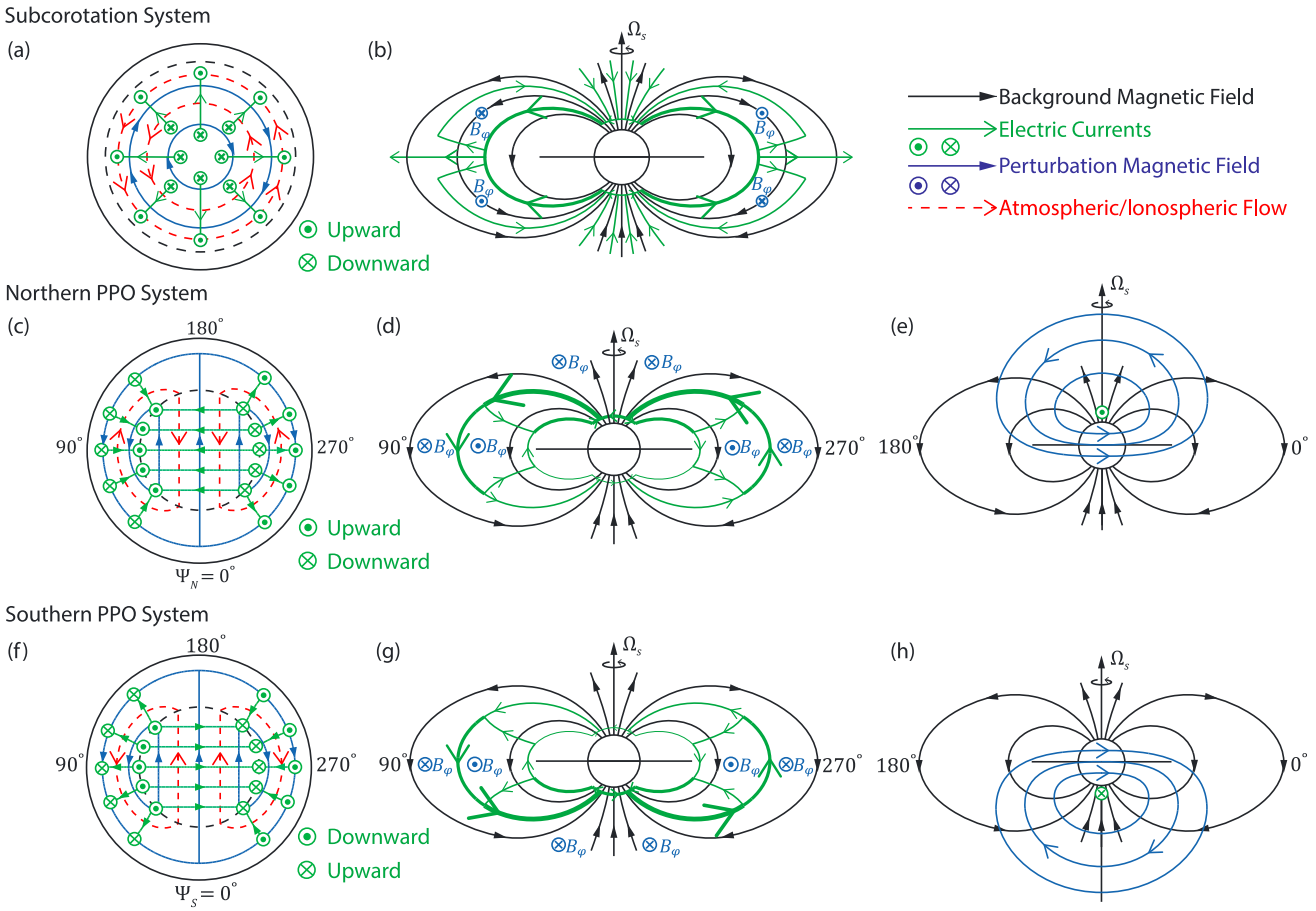

Figure 1. Sketches showing the form of the electric currents and perturbation magnetic fields associated with Saturn plasma subcorotation and the PPO-related current systems. Black arrowed lines indicate the background magnetic field, green arrowed lines and symbols the electric current system, and blue arrowed lines and symbols the associated perturbation magnetic field. Circled dots and crosses indicate vectors pointing out of and into the plane of the diagrams, respectively. The red arrowed dashed lines in the ionospheric diagrams on the left show the associated upper atmospheric and ionospheric flow, where those in the PPO-related diagrams assume that these systems are driven from the atmosphere. (a and b) The current system associated with magnetospheric plasma subcorotation, where Figure 1a shows the northern ionosphere viewed looking down from the north and Figure 1b shows a view in a magnetic meridian plane. The system is assumed axisymmetric to a first approximation. (c-e) The northern PPO-related system, where Figure 1c shows the northern ionosphere viewed looking down from the north, Figure 1d the $\Psi_N = 90° - 270°$ meridian plane, and Figure 1e the $\Psi_N = 0° - 180°$ meridian plane. (f-h) The southern PPO-related system, where Figure 1f shows the southern ionosphere viewed through the planet looking down from the north, Figure 1g the $\Psi_S = 90° - 270°$ meridian plane, and Figure 1h the $\Psi_S = 0° - 180°$ meridian plane.

symbols the current system, and the blue arrowed lines and symbols the perturbation field associated with that current system, while in the ionospheric diagram the red dashed lines show the associated atmospheric/ionospheric flow. Circled dots and crosses indicate vectors pointing out of and into the plane of the diagrams, respectively.

Figures 1a and 1b show the basic form of the current system and field perturbations associated with plasma subcorotation, where Figure 1a shows a view looking down on the northern ionosphere from above, while Figure 1b shows a view in a meridian plane. Subcorotation in Saturn's magnetosphere results from the ionization, pickup, and outward transport of plasma originating from the neutral water gas emitted by the moon Enceladus, which orbits deep within the magnetosphere at a radial distance of ~4 R_s [e.g., *Pontius and Hill*, 2009]. (R_s is Saturn's 1 bar equatorial radius, equal to 60,268 km.) Observationally, compared with a planetary rotation period of ~10.65 h, the angular velocity of the equatorial plasma is found to fall monotonically from near rigid corotation at ~3 R_s, to ~70–80% of rigid corotation at ~10 R_s, and to ~50–60% of rigid corotation at ~20 R_s [*Wilson et al.*, 2008, 2009; *Müller et al.*, 2010; *Thomsen et al.*, 2014; *Carbary and Mitchell*, 2014], while spectroscopic observations of infrared aurora indicate typical values of ~30-50% of rigid corotation at polar latitudes [*Stallard et al.*, 2004, 2007]. Given the sense of Saturn's internal magnetic field as shown in Figure 1,

subcorotation at high latitudes first implies the presence of distributed downward currents in the polar region in both hemispheres, as in the models of *Cowley and Bunce* [2003] and *Cowley et al*. [2004a, 2004b, 2008]. These downward currents feed equatorward-directed Pedersen currents in the northern and southern ionospheres that increase with distance from the pole due to both the increasing neutral-plasma relative velocity with distance from the pole, and the expanding spherical geometry of the system. The ionospheric currents then close within the magnetosphere via a more latitudinally restricted ring of upward directed field-aligned current as the plasma angular velocity returns toward rigid corotation. The details evidently depend on the latitudinal plasma angular velocity profile, resulting in the main upward current flowing near the open-closed field boundary (OCB) in the above theoretical models, while the results of *Hunt et al*. [2014] have shown that the ionospheric conductivity profile is equally important, resulting in the upward current region being displaced slightly equatorward of that boundary in the nightside data they examined. We note that a second ring of weaker upward current also occurs in the theoretical models at lower latitudes, which appears to have no counterpart in the observed system (see section 4.5). The associated magnetic perturbations in the subcorotating region (blue symbols in Figures 1a and 1b) are directed azimuthally, negative in the northern hemisphere with respect to the northern spin/magnetic axis and positive in the southern. (We note that the spin and planetary magnetic axes are co-aligned at Saturn to within ~0.1° [*Burton et al*., 2010].) In the closed field region the field lines are consequently bent out of meridian planes into a "lagging" field configuration, while in the open field region the field becomes twisted within each tail lobe [*Isbell et al*., 1984]. We note, however, that should some process cause the plasma to rotate faster than the neutral atmosphere, the sense of the current system and magnetic field perturbations would reverse, producing in that case a "leading" field configuration on closed field lines.

Figures 1c–1h similarly show the current systems and field perturbations associated with the PPOs [*Southwood and Kivelson*, 2007; *Andrews et al*., 2010b; *Southwood and Cowley*, 2014], where Figures 1c–1e relate to the northern system and Figures 1f–1h to the southern. The format follows that for the subcorotation system described above, on the left showing views from the north of the northern and southern ionospheres, viewed "through" the planet in the latter case, while on the right showing conditions in two orthogonal principal meridians as described below. The principal currents in both cases flow into the corresponding auroral ionosphere (north or south) on one side, across the polar region as a Pedersen current, and out of the other, closing partially within the equatorial plasma, partly as a weaker interhemispheric current in the opposite hemisphere, and partly through field-aligned currents at lower latitudes. Analysis of equatorial Cassini magnetic field data obtained during 2004–2007, before the 2008 high-latitude interval examined here, shows that the outer system of field-aligned currents were located on the nightside at ~15 R_s in the equatorial region, while the weaker inner field-aligned currents were located inside ~5 R_s [*Andrews et al*., 2010a]. Azimuthal location with respect to these two current systems is defined in terms of two phase functions, Ψ_N for the northern system and Ψ_S for the southern as indicated in Figures 1c and 1f, respectively. These will be employed extensively throughout this paper. It should be noted that the two phases have the same values with respect to the senses of the magnetic field perturbations shown in the diagrams, and hence with the physical direction of the associated current flow. We note, however, that the field-aligned currents have opposite directions with respect to the ionosphere in the two cases (both being viewed from the north). Thus, in the northern hemisphere in Figure 1c the main (poleward) field-aligned current is directed out of the ionosphere at $\Psi_N = 90°$ and into the ionosphere at $\Psi_N = 270°$, while in the southern hemisphere in Figure 1f the main field-aligned current is directed out of the ionosphere at $\Psi_S = 270°$ and into the ionosphere at $\Psi_S = 90°$. We note that the associated twin-vortical atmospheric/ionospheric flows shown by the red dashed lines in these figures assume that the system is driven from the atmosphere, as for the subcorotation flows. This is consistent with the recent modeling assumptions of *Jia et al*. [2012] and *Jia and Kivelson* [2012], and the prior results of *Hunt et al*. [2014]. Figures 1d and 1e then show the northern system currents and field perturbations in the 90°-270° and 0°-180° meridians, respectively, as indicated in the figure, while Figures 1g and 1h similarly show the currents and perturbation fields for the southern system. In both cases the current system produces a quasi-uniform perturbation field in the equatorial region that points radially (r) outward at $\Psi_{N,S} = 0°$ and inward at 180° (Figures 1e and 1h) and has positive and negative azimuthal (φ) field components at $\Psi_{N,S} = 90°$ and 270°, respectively (Figures 1d and 1g). Combined with the background planetary field, this quasi-uniform perturbation field produces an effective tilting of the magnetic equator, and a north-south displacement of the plasma sheet in the tail [e.g., *Provan et al*., 2012, and references therein]. These

perturbation fields then close in both the equatorial region outside of the main field-aligned current region (Figures 1d and 1g), as well as over the pole corresponding to that current system (Figures 1e and 1h), where the azimuthal field has the opposite sense at a given phase $\Psi_{N,S}$ to that in the inner equatorial region, forming a region of quasi-dipolar field transverse to the planetary dipole. As indicated in Figures 1e and 1h, a colatitudinal (θ) component of the perturbation field is also present, consistent with the large-scale perturbation field loops shown in these diagrams.

Each of these two systems then rotates at similar but separate periods close to the planetary rotation period, that have been found, initially through tracking related modulated radio wave emissions, to vary slowly with Saturn's seasons [*Galopeau and Lecacheux*, 2000; *Kurth et al*., 2008; *Gurnett et al*., 2009a, 2009b, 2011; *Lamy*, 2011]. Essentially the same rotation periods have been derived by following the phase of the resulting magnetic field oscillations observed during periapsis passes of the Cassini spacecraft [*Andrews et al*., 2008, 2010b, 2012; *Provan et al*., 2014]. During the interval of interest here spanning 2008, occurring somewhat before Saturn equinox in mid-August 2009, the northern and southern periods were well separated at ~10.60 and ~10.82 h, respectively. At a given point in the equatorial region inside the main field-aligned current sheets the azimuthal field of each system thus oscillates in lagging quadrature with the radial component, this being the signature of a quasi-uniform perturbation field in the near-equatorial region, while outside the current sheets the sense of the azimuthal field is reversed so that it oscillates in leading quadrature with the radial, this being the signature of a quasi-dipolar field [*Espinosa and Dougherty*, 2000; *Espinosa et al*., 2003; *Cowley et al*., 2006; *Southwood and Kivelson*, 2007; *Andrews et al*., 2008, 2010a; *Provan et al*., 2009]. The colatitudinal component then oscillates in antiphase with the radial in the northern system and in-phase with the radial in the southern, as is evident in Figures 1e and 1h. The field perturbations of both systems are superposed and interfere in the equatorial region, producing beats with a period of ~22 days during the interval examined here [*Provan et al*., 2011], but have been found to be pure northern and southern in the corresponding polar region, to within an ~10% observational limit by amplitude [*Andrews et al*., 2012].

It should thus be noted for future reference that the azimuthal PPO perturbation field, the component employed here to study the field-aligned currents in the auroral region, varies with azimuth around each system to a first approximation as ~ sin $\Psi_{N,S}$ in the equatorial region inside the main field-aligned currents, and as ~ –sin $\Psi_{N,S}$ in the outer equatorial and polar regions, the switch between the two being associated with the PPO-related field-aligned current flow through Ampère's law. The radial component similarly varies throughout as ~ cos $\Psi_{N,S}$. Empirically, the orientation of each current system at any time is defined through the phase functions $\Phi_{N,S}(t)$ which give the azimuth φ with respect to noon (increasing in the sense of planetary rotation) in which the quasi-uniform equatorial perturbation field points radially outward, thus corresponding to $\Psi_{N,S} = 0°$ in Figures 1c–1h. The value of $\Psi_{N,S}$ at any other azimuth φ is then given by

$$\Psi_{N,S}(\varphi, t) = \Phi_{N,S}(t) - \varphi. \tag{1}$$

As in *Hunt et al*. [2014], the phases $\Phi_{N,S}(t)$ employed here are those determined by *Andrews et al*. [2012], obtained from running ~200 day fits to Cassini magnetic oscillation data. The periods of the northern and southern oscillations are correspondingly given by

$$\tau_{N,S}(t) = \frac{360}{\left(\frac{d\Phi_{N,S}}{dt}\right)}, \tag{2}$$

where $\Phi_{N,S}(t)$ are expressed in degrees.

As indicated above, *Hunt et al*. [2014] investigated the magnetic perturbations associated with field-aligned currents in the nightside southern hemisphere on a sequence of near-polar Cassini orbits in 2008. It was found that the form of the currents was well organized by the southern PPO phase and that these PPO-related variations give rise to the differing current morphologies noted previously by *Talboys et al*. [2009, 2011] in initial study of this data. No obvious evidence was found for a strong influence at the northern period, the hypothesized interhemispheric currents shown in Figures 1d and 1g not withstanding. It was also found that the rotating PPO field-aligned currents were essentially co-located with the main upward current region of the PPO-independent subcorotation system, and of approximately equal strength. Thus, when the PPO-related currents were also directed upward the net current within the auroral current layer was approximately doubled, while when it was directed downward the net current was reduced to near zero, although individual

layers of upward and downward current remained present. In this paper we newly examine the northern hemisphere data in these terms and show that both northern and southern period currents were present in this case, thus providing the first direct evidence for the PPO-related interhemispheric currents hypothesized by *Southwood and Kivelson* [2007]. We also further reexamine the southern data for evidence of northern period currents and show that weaker effects are indeed present.

2. Data Set and Analysis Procedure

2.1. Data Set

The data set and analysis procedures employed in this paper have been fully described and justified in section 2 and the appendices of *Hunt et al.* [2014], such that only a brief outline of the main features will be provided here. The data originate from a set of periapsis passes of the Cassini spacecraft, which were sufficiently inclined to the equatorial plane that the trajectory passed over the northern and southern nightside auroral regions at radial distances ~3–5 R_S. The orbits concerned are Revs 59–95, inclusive, occurring between February and December 2008. Of the 37 northern inbound passes examined here, one (Rev 71) is missing due to an extended data gap, while two others (Revs 84 and 89) have been excluded from the study as showing unusually large signatures that do not follow the general trends. One of the latter, Rev 89, has previously been the subject of special examination as a case likely associated with a major compression of the magnetosphere by the solar wind [*Bunce et al.*, 2010]. In this study we also further examine and compare these data with the southern outbound passes studied by *Hunt et al.* [2014], two of which (Revs 70 and 71) are missing due to data gaps, while four (Revs 66, 77, 89, and 94) were similarly excluded as showing atypical signatures. Here we thus employ the data from 34 northern and 31 southern passes over Saturn's nightside auroral regions.

The periapsis segments of three representative Revs are shown in Figure 2 in *KGS* coordinates, where the *Z* axis is Saturn's spin/magnetic axis, the *X-Z* plane contains the Sun, and *Y* completes the right-handed triad pointing toward dusk. The Revs shown are 60, 76, and 93 spanning the interval of the study, shown by the blue, green, and red lines, respectively. Figures 2a and 2b show the trajectories projected onto the *X-Z* (noon-midnight) and *X-Y* (equatorial) planes, respectively, where solid circles are plotted every 3 h along the trajectories, labeled with the "day of year" number at the start of each day. The near-polar nature of these orbits is evident, with periapsis just south of the equator in the premidnight sector, such that the inbound northern polar passes in the premidnight sector occur at slightly larger radii than the southern outbound polar passes in the midnight and postmidnight sector.

In Figures 2c and 2d we show the northern and southern segments of these trajectories mapped along model field lines into the northern and southern ionospheres, respectively, starting from the near-periapsis point where the mapped northern and southern colatitudes are simultaneously the largest with respect to the corresponding poles (i.e., where the trajectory mapped into a meridian is tangent to the field lines). The view is from the north in both cases, thus through the planet in Figure 2d, as in Figure 1, with dusk at the top and noon to the right. Dotted latitude circles and longitude lines are shown at intervals of 5° and 3 h LT, respectively. As in *Hunt et al.* [2014], the magnetic model employed consists of the three-term axisymmetric *Burton et al.* [2010] model of the internal planetary field together with the empirical *Bunce et al.* [2007] ring current model appropriate to a fixed intermediate subsolar magnetopause distance of 22 R_S. The "ionosphere" corresponds to the surface 1000 km above the International Astronomical Union (IAU) reference spheroid [*Galand et al.*, 2011], which has equatorial and polar radii of 61,268 and 55,364 km, respectively. We also show in these figures the mean northern and southern auroral "ovals" obtained from Cassini Ultraviolet Imaging Spectrograph (UVIS) data by *Carbary* [2012]. The center line with black circles indicates the location of maximum mean auroral emission, while the lines on either side show the half-intensity points. It can be seen that the inbound passes crossed through the northern mean auroral region in the postdusk to premidnight sector, where the oval is centered at ~15° colatitude, while the outbound passes similarly crossed the auroral region in the southern midnight to postmidnight sector, where the oval is centered at ~17.5° colatitude. The difference in colatitude is principally a result of the north-south asymmetry in the planetary magnetic field associated with the axial quadrupole field [*Burton et al.*, 2010], which results in northern field lines mapping closer to the pole by a degree or two compared with their southern counterparts.

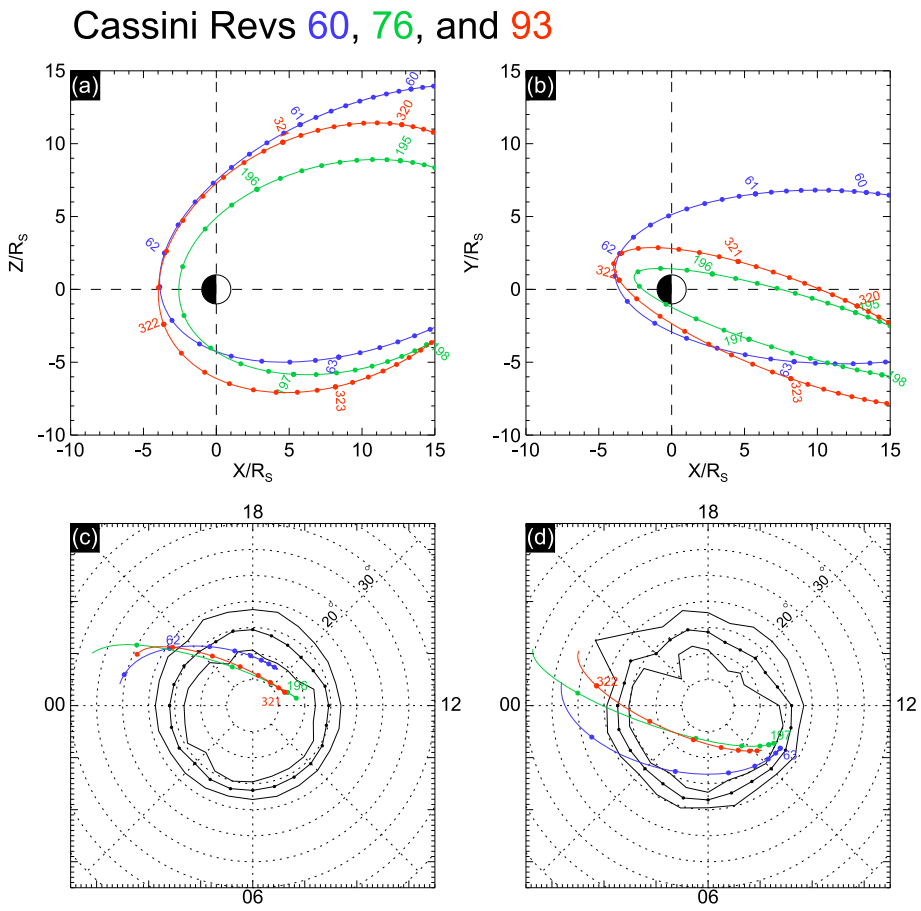

Figure 2. Periapsis segments of three Cassini Revs from near the beginning (Rev 60, blue), middle (Rev 76, green), and end (Rev 93, red) of the interval studied in this paper, shown projected into (a) the *X-Z*, and (b) the *X-Y* planes in KGS coordinates (*Z* points along Saturn's spin/magnetic axis, the *X-Z* plane contains the Sun, and *Y* completes the right-hand triad pointing to dusk). Solid circles are plotted at 3 h intervals, labeled with the day of year number (2008) at the start of each day. (c and d) The northern inbound and southern outbound segments of these trajectories are projected along model magnetic field lines into the northern and southern ionospheres, respectively, the trajectories being divided at the near-periapsis point on the left of each plot where they achieve their largest colatitude with respect to both northern and southern poles. The view is from the north in both cases, thus through the planet in Figure 2d, with dusk at the top and noon to the right. A dotted grid of 5° in colatitude and 3 h in LT is also shown. The magnetic mapping employed is described in section 2.1. The black lines in Figures 2c and 2d show the statistical location of the northern and southern UV auroral ovals, respectively, derived by *Carbary* [2012] from Cassini UVIS data obtained over the same interval. The dotted center line shows the position of peak intensity, while the outer and inner lines show the half power points.

2.2. Data Analysis Procedures

The initial data set employed consists of 1 min averaged values of the azimuthal magnetic field component B_φ, which, as outlined in section 1, contains the primary signatures of the field-aligned currents associated with magnetosphere-ionosphere coupling. The first step in the analysis is to estimate and remove the contribution to this component produced by other current sources. Due to their axisymmetry, however, no contribution is made by either of the primary fields observed by the spacecraft on these periapsis segments, namely, the internal planetary field and the ring current field [*Burton et al.*, 2010; *Kellett et al.*, 2011], as employed, for example, in the field mapping in Figure 2. The main magnetospheric contribution to the azimuthal field instead comes from the magnetopause and tail current system, which bends field lines out of meridian planes from the dayside toward the tail on both sides of the noon-midnight meridian. These fields have been estimated using the paraboloid model of Saturn's magnetic field, specifically the "intermediate" model for a subsolar magnetopause distance of 22 R_s [*Belenkaya et al.*, 2008]. These values have thus been routinely computed for each Cassini pass employed here and subtracted from the initial data, such that all future reference in the paper to the "azimuthal field" and products derived therefrom implies use of these

"corrected" data. As shown in *Hunt et al*. [2014, Appendix A], however, for these observations in the vicinity of the noon-midnight meridian the correction fields are typically of magnitude ~1 nT or less, compared with observed signatures of order ~10 nT, so that the correction is generally small.

The second step is to map the azimuthal field values along field lines down to the ionosphere, using the same model field and ionospheric height as employed to produce Figures 2c and 2d. This step normalizes the data obtained at modestly varying radial distances between ~3 and ~5 R_s from pass to pass (Figure 2) and provides the means to directly address the issue of related meridional ionospheric currents. To map the field we assume that ρB_φ is constant along background field lines between the field-transverse closure currents in the ionosphere at one end and in the magnetosphere at the other, where ρ is the perpendicular distance from the spin/magnetic axis of the planet. In *Hunt et al*. [2014, Appendix B] this assumption is shown to be exact in the case of an axisymmetric current system such as the ideal plasma subcorotation current illustrated in Figures 1a and 1b and also to be approximately true for the PPO-related current systems illustrated in Figures 1c–1h. The estimated azimuthal field just above the ionosphere is thus given by

$$B_{\varphi i} = B_\varphi(\rho/\rho_i), \tag{3}$$

where ρ_i is the perpendicular distance of the field line foot in the ionosphere.

Third, given $B_{\varphi i}$, the meridional height-integrated ionospheric current in Ampères per meter of azimuth that switches off this field underneath the ionosphere is given from Ampère's law by

$$i_m = \mp B_{\varphi i}/\mu_o, \tag{4}$$

where μ_o is the permeability of free space. Here the upper sign corresponds to the northern hemisphere and the lower to southern, where the current is taken to be positive when directed from the pole to the equator in both hemispheres. The primary current parameter employed here, however, is not the current per meter of azimuth i_m, but the current per radian of azimuth I_m, given by

$$I_m = \rho_i i_m = \mp \rho_i B_{\varphi i}/\mu_o = \mp \rho B_\varphi/\mu_o, \tag{5}$$

where we have used equation (3), and I_m is again taken to be positive directed from pole to equator in both hemispheres. The field-aligned current density just above the ionosphere is then given by current continuity as

$$j_{\parallel i} = \mp \frac{1}{\rho_i \cos\alpha_i}\left[\frac{\partial I_m}{\partial s_m} + \frac{\partial i_\varphi}{\partial \varphi}\right], \tag{6}$$

where the upper and lower signs again refer to the northern and southern hemispheres and the sign of the field-aligned current is with respect to the direction of the background field, such that, for example, positive $j_{\parallel i}$ implies an upward current with respect to the ionosphere in the northern hemisphere but a downward current in the southern hemisphere. In this equation α_i is the angle of the background field to the local vertical (independent of field direction), i_φ is the azimuthal ionospheric current per meter of colatitude, and s_m is the meridional path length in the ionosphere taken positive from the corresponding pole toward the equator ($ds_m \approx R_{pi} d\theta_{iN,S}$ near the northern and southern poles, where R_{pi} is the polar radius of the ionosphere and $d\theta_{iN,S}$ is the colatitude measured from the corresponding pole).

We note from equation (6) that in the limit that the second term on the right side can be neglected, the field-aligned current density is simply given by the meridional gradient of I_m. When this condition is satisfied, the total field-aligned current per radian of azimuth flowing between meridional positions s_{m1} and s_{m2} (with $s_{m2} > s_{m1}$) is given by

$$I_\parallel \approx \mp(I_m(s_{m2}) - I_m(s_{m1})), \tag{7}$$

a quantity that is then fixed on the background field lines concerned between the ionosphere and the region of field-transverse closure current in the magnetosphere. Here again the upper and lower signs are appropriate to the northern and southern hemispheres, and the sign of the current is with respect to the direction of the background field. In Appendix C of *Hunt et al*. [2014] it was shown on both theoretical and empirical bases that when the gradient in the first term in equation (6) exceeds ~0.3 MA rad^{-1} per degree of colatitude, the second term should be at least an order of magnitude less than the first, and hence negligible, such that equation (7) should then be applicable. It was also found that such a gradient appropriately distinguishes between the strong field and current gradients typical of the auroral region

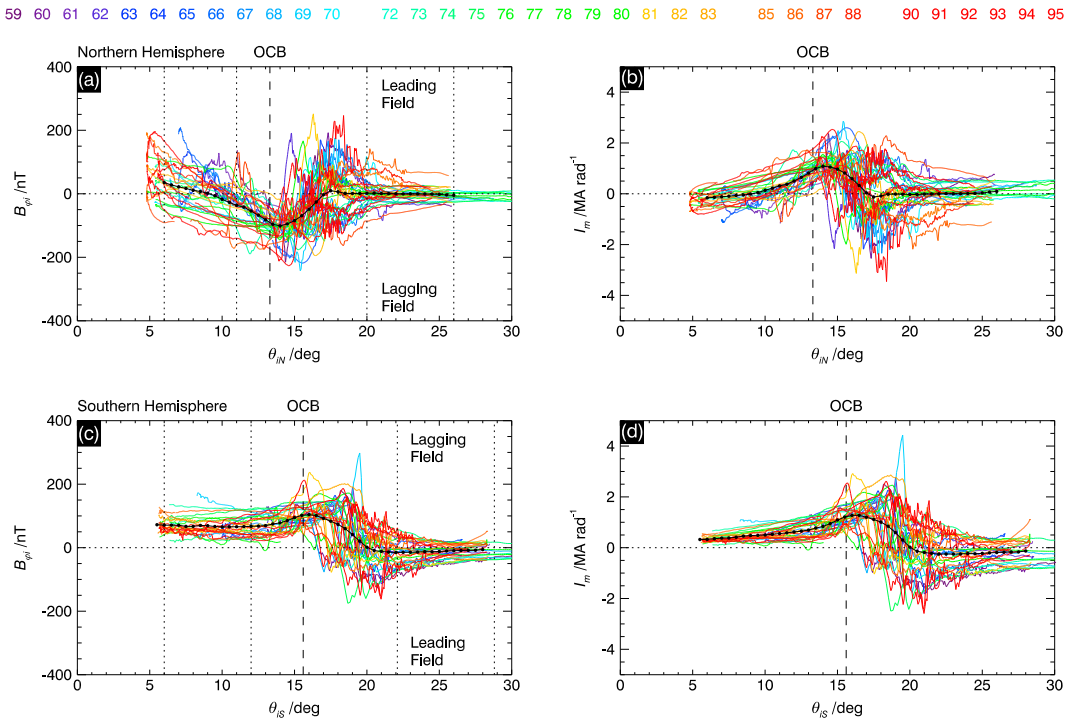

Figure 3. (a) A composite plot of all the corrected northern hemisphere azimuthal field data, $B_{\varphi i}$ (nT), mapped to the northern ionosphere using equation (3) and plotted versus colatitude from the northern pole, θ_{iN} (deg). The data profiles are color-coded by Cassini Rev as shown at the top of the figure. The black solid circles joined by black lines show averages obtained in overlapping 1° colatitude bins every 0.5°, derived as described in section 3.1. (b) Similarly shows the corresponding northern meridional current profiles, I_m (MA per radian of azimuth), obtained using equation (5). (c and d) The corresponding southern hemisphere azimuthal field and meridional current profiles, mapped into the southern ionosphere and plotted versus colatitude from the southern pole, θ_{iS} (deg). The averaged colatitude of the OCB from *Jinks et al.* [2014] is also marked at the top of each plot and by the vertical dashed lines. The vertical dotted lines in Figures 3a and 3c show the colatitude intervals used in the polar and equatorial ranges in Figure 5. In Figures 3a and 3c we indicate which signs of $B_{\varphi i}$ correspond to lagging and leading fields in each hemisphere.

that satisfy this criterion, and those at higher and lower latitudes that typically do not. This limit will thus again be employed here as a guide to the validity of the approximation given in equation (7).

3. Overview of Northern Hemisphere Data

3.1. Initial Overview and PPO-Independent Perturbations

In this section we first overview the northern hemisphere data to be analyzed in greater detail in subsequent sections and begin in Figure 3 by showing overall colatitude profiles combining and averaging all the mapped data from the Revs included as indicated in section 2.1. We also show for comparison corresponding plots of the southern data, not shown in this form by *Hunt et al.* [2014]. Figures 3a and 3b thus show the northern $B_{\varphi i}$ profiles obtained from the (slightly corrected) observed data using equation (3), and the corresponding I_m profiles obtained from equation (5), respectively, both plotted versus colatitude from the northern pole. Figures 3c and 3d show the corresponding southern $B_{\varphi i}$ and I_m profiles, both plotted versus colatitude from the southern pole. The averaged position of the OCB in each hemisphere determined by *Jinks et al.* [2014] is indicated for future reference by the vertical dashed lines, located at 13.3° in the north and 15.6° in the south. (The vertical dotted lines in Figures 3a and 3c also indicate the polar and equatorial regions whose field data are employed in the analyses in sections 4.1 and 4.4.) The data from each Rev are color-coded according to the scheme at the top of the figure, while the black solid circles joined by straight lines show values averaged in overlapping 1° colatitude bins evaluated every 0.5°. We note that the density of data values per degree varies significantly from pass to pass due to the varying radial distance and hence speed of the spacecraft. In order to avoid the averages being overly dominated by contributing Revs with

the highest density of data points, we first average all the data from a given Rev contributing to a colatitude bin, and then derive a weighted average over all the contributing Revs as shown. The chosen weights are logarithmic, $W = \log_{10} N$, where N is the number of data points contributed to a bin from a given Rev, such that the weight of a single data point is taken to be zero, while an average obtained from 10 points has a weight of one, and that from a hundred points a weight of two. All of the related averaged profiles in this paper have been derived using this method.

In considering these profiles we recall from Figure 1 that lagging fields correspond to negative $B_{\varphi i}$ in the northern hemisphere and positive $B_{\varphi i}$ in the southern, as indicated in Figure 3, with positive equatorward directed I_m in both hemispheres (equation (5)). Oppositely signed fields with negative poleward directed currents then correspond to leading fields. On the assumption that the oscillatory PPO-dependent contributions average to small values over random northern and southern PPO phases, we might expect that the averaged profiles in Figure 3 represent a first, smoothed, approximation to those associated with the PPO-independent currents, with dominant lagging fields in both hemispheres if these are associated with plasma subcorotation as expected. Assuming that azimuthal Pedersen currents can be neglected for such near-axisymmetric subcorotation currents, we note that I_m increasing with colatitude implies downward field-aligned current into the ionosphere as given by equation (7), while I_m decreasing with colatitude implies upward field-aligned current out of the ionosphere. Variations about the mean values in Figure 3 then represent the effect of the PPO-related currents, together, of course, with any other natural variations in the system, such as changes in the colatitude of the auroral region associated with changes in the amount of open flux present.

If we first examine the southern profiles in Figures 3c and 3d, it can be seen that the azimuthal field and related meridional current are consistently positive (lagging) at the smallest southern colatitudes observed, implying subcorotation of the polar plasma. With increasing colatitude the averaged current increases in strength, more rapidly near ~15° together with the azimuthal field, and peaks at ~1.3 MA rad^{-1} near ~16.5°, just equatorward of the averaged OCB, thus implying a total distributed downward current over the whole polar region of ~8 MA assuming axisymmetry. The field and current then fall between ~17° and ~20° to small negative averaged values, associated with an upward current layer that closes essentially all of the polar current, beyond which the field-aligned currents remain negligible in the region observed. We note that this behavior is entirely consistent with the averaged PPO-independent current profiles derived through more detailed analysis in *Hunt et al.* [2014] (see their Figures 9 and 15). The variations about the mean field values at smallest and largest colatitudes then imply the presence of PPO-related oscillations of amplitude ~20–30 nT in these regions, also consistent with the results of *Hunt et al.* [2014] (see their Figure 5). The variations within the main current region, however, are notably larger, ~100 nT in amplitude.

With regard to the small negative (leading) averaged values of the field and current at largest colatitudes in Figures 3c and 3d, these might be taken from the above discussion as indicating the presence of weak supercorotation of the plasma in the inner magnetosphere region. However, as noted in section 1, the observed plasma rotation velocities are consistently subcorotating on corresponding field lines (mapping in the equatorial plane inside of ~9 R_s), which makes this association highly unlikely. Instead, these weak averaged leading field values were suggested in *Hunt et al.* [2014] to be due to lack of perfect antisymmetry in the PPO-related fields, with positive values being slightly larger than the negative values during each PPO oscillation cycle as a result of related spatial oscillations in the location of the currents.

Now examining the northern data in Figures 3a and 3b, it can be seen to a first approximation that these are similar in form to those in the south, but with the averaged $B_{\varphi i}$ profile in Figure 3a inverted to predominantly negative lagging values, overall consistent with a subcorotation origin. The main meridional currents in Figure 3b remain positive, directed equatorward, as in the south. Overall, therefore, the profiles are similarly consistent with a distributed downward current of ~7 MA flowing into the polar region, the peak current being ~1.1 MA rad^{-1} at ~14° colatitude again just equatorward of the averaged OCB, closed by a narrower layer of upward current at larger colatitudes. However, some points of comparison should be made. First, the main layer of upward current is located between ~15° and ~17° colatitude in the north compared with ~17° and ~20° in the south, this difference again reflecting the axial quadrupole asymmetry in the background planetary field noted in section 2.1 above. As may be expected, these regions of upward current are quite consistent with the positions of the averaged UV auroral ovals determined by *Carbary* [2012] shown in Figures 2c and 2d, thus justifying our use of the term "auroral" for these current regions. Second, while in

the southern hemisphere the PPO-related oscillations in the region poleward of the main upward currents are superposed on a consistently lagging field suggesting plasma subcorotation over the whole polar region, the averaged polar perturbations in the north drop to small values poleward of ~10° colatitude, and indeed switch sign to become weakly leading in nature at the smallest colatitudes observed. Since supercorotating flows at polar colatitudes again seem implausible, this again suggests an origin in a lack of exact antisymmetry in the PPO-related perturbation fields. It is evident, however, that the lagging field associated with plasma subcorotation is generally much weaker in the north polar region than in the south. We note in this context that the passes employed in this study were obtained ~1 year before Saturn equinox in August 2009, when Saturn's northern spin axis was on average inclined ~6° away from the Sun (between ~8° and ~4° over the interval). The region poleward of ~10° in the southern hemisphere was thus mostly or wholly illuminated by the Sun during each planetary rotation, while the equivalent region in the north was mostly or wholly unilluminated. The above differences in the polar data may thus relate to much weaker polar ionospheric conductivities in the north compared with the south during this interval [*Galand et al*., 2011].

3.2. Rev-by-Rev Survey and PPO-Related Perturbations

While the field and current profiles in Figure 3 indicate the range of the PPO-related field and current variations about the mean values, we now wish to make an initial but more detailed investigation of these variations by examining the field perturbations on individual passes in relation to the concurrent PPO phases. While the southern signatures were found by *Hunt et al*. [2014] to be well organized by the southern PPO phase throughout, the field perturbations in the northern hemisphere appear to be organized by the northern phase in the polar region poleward of the main upward current region, but to be influenced by both northern and southern phases in the equatorward region. Initial evidence on which this conclusion is based is shown in Figure 4, where we show data plotted versus northern mapped ionospheric colatitude from 6 of the 34 passes employed in the study, chosen to illustrate a range of conditions of the two PPO phases. Specifically, we have chosen cases in which the main PPO-related currents of the northern and southern systems should both have the same sense according to Figure 1, either upward or downward (Figures 4a and 4b), or have opposite senses to each other (Figures 4c and 4d), or where both PPO systems should be close to zero potentially exhibiting the PPO-independent profile (Figure 4e). We also show one of four passes that exhibits unusual behavior having no clear counterpart in the southern data studied by *Hunt et al*. [2014] (Figure 4f). In each panel of the figure we show from top to bottom (i) a Cassini plasma spectrometer-Electron Spectrometer (CAPS-ELS) electron count rate spectrogram covering the energy range ~0.6 eV–28 keV, color-coded as shown at the upper right of the figure; (ii) the ionospheric meridional Pedersen current I_m (MA rad^{-1}) derived as in Figure 3 using equation (5); and (iii) the northern (blue line) and southern (red line) PPO phases, $\Psi_{N,S}$ (degrees), obtained from equation (1) using the phases determined by *Andrews et al*. [2012]. Vertical dashed lines in the figure indicate the principal field-aligned current layers identified from sequential extrema in the I_m profiles, all of which satisfy the significance criterion discussed in section 2.2. These lines are shown generally in green, but with those bracketing the principal layer of upward current being shown purple. We note that in the lower panels the PPO phases increase significantly with time and hence colatitude from left to right on these northern inbound trajectories (see Figure 2), with changes in value exceeding ~180° in each case. Unlike the more rapid passes at lower altitudes across the southern auroral region (Figure 2) therefore the northern passes cannot be regarded as occurring at almost fixed values of PPO phase (compare, e.g., with Figure 4 of *Hunt et al*. [2014]).

If we first examine the current profiles at smallest colatitudes, between ~5° and ~10°, it can be seen that overall these correspond to expectations based on the concurrent northern PPO phase, i.e., positive values for phases between 0° and 180° via peak values at ~90° and negative values for phases between 180° and 360° via peak values at ~270° (see the blue and green lines in Figure 1c in the polar region, noting that $B_{\varphi i}$ and I_m always have opposite signs in the northern hemisphere). Thus, for example, we see negative values of I_m in this regime for $\Psi_N \sim 270°$ in Figure 4e, positive values for Ψ_N ~90° in Figure 4f, and changes from negative toward positive as Ψ_N increases from ~270° through 360°/0° toward ~90° in Figure 4b. Senses opposite to those observed would have been found, e.g., in Figures 4c and 4e, if the field perturbations in this regime had been responding to the southern PPO phase. Similar results were found by *Hunt et al*. [2014] in the southern polar region with respect to the southern PPO phase, but superposed in that case on a larger PPO-independent positive meridional current (lagging field) that to a first approximation is absent at similar colatitudes in the north, as seen in Figure 3.

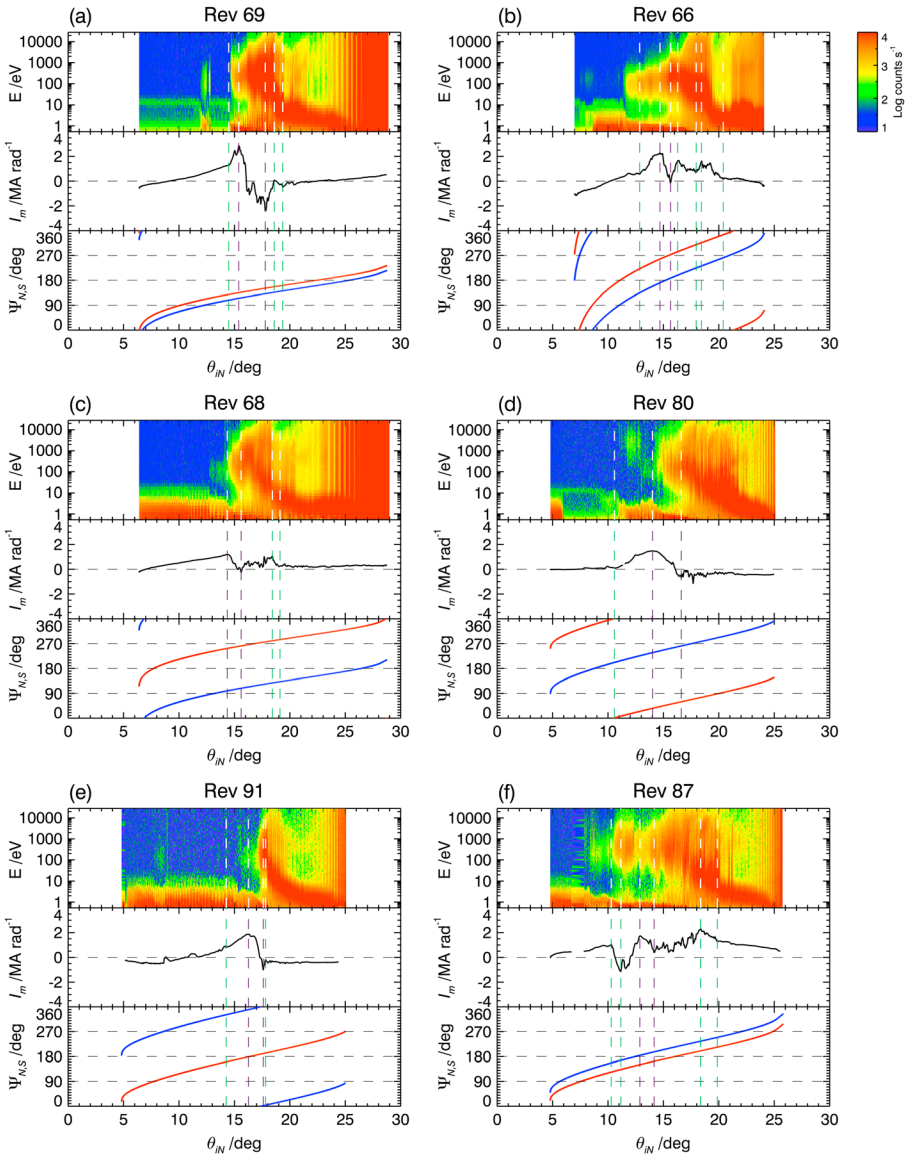

Figure 4. Data are shown from the northern inbound passes of six Cassini Revs, as marked at the top of each figure, chosen to exemplify differing conditions of the PPO-related phases. From top to bottom, each panel of the figure shows (i) a CAPS/ELS electron count rate spectrogram covering the energy range ~0.6 eV–28 keV, color-coded as shown at upper right; (ii) the ionospheric meridional current, I_m (MA rad^{-1}), derived from magnetic field data using equation (5); and (iii) the two PPO-related phases, Ψ_N (deg) shown by the blue line and Ψ_S (deg) shown by the red. Spacecraft position has been mapped along model field lines to the northern ionosphere as described in section 2.2, with parameters being plotted versus colatitude measured from the northern pole. Vertical dashed lines indicate the principal field-aligned current sheets drawn between extrema in the I_m data with overall gradients meeting or exceeding the limit discussed in section 2.2. These are shown generally in green, but with the principal upward current region being bracketed by the purple lines. I_m values increasing or decreasing with colatitude indicate downward or upward currents, respectively. In the polar region the intense electron fluxes at energies below ~10 eV are spacecraft photoelectrons, observed where the spacecraft potential is positive relative to the external medium. These disappear around ~18° colatitude as the spacecraft encounters the cool dense plasma of the inner magnetosphere nearer the equator, and charges to a negative potential. The high energy-independent counts recorded equatorward of ~23° colatitude are due to penetrating radiation belt particles, striped due to instrument scanning. The panels of the figure have been chosen to illustrate various conditions of the northern and southern PPO phases in the auroral current sheet region. (a and b) Cases where the main PPO currents are expected to have the same sense as each other according to Figure 1, with both PPO phases being the in 180° range centered on 90° (both up currents) in Figure 4a, and both being in the 180° range centered on 270° (both down currents) in Figure 4b. (c and d) Cases where the two PPO currents should be opposite, up for the northern and down for the southern in Figure 4c, and vice versa in Figure 4d. (e) A case in which the northern and southern PPO currents should both be small in the auroral region, with phases in the vicinity of ~180° or 0°/360°. (f) One of four cases with hot plasma and field-aligned current at unusually high latitudes.

Beyond ~10° colatitude, however, an upward trend in positive I_m (lagging field) values becomes evident in all cases irrespective of the PPO phases (an exception being Figure 4f discussed separately below), as also seen in the averaged profile in Figure 3b, which appears generally to begin on open field lines as judged from the absence of hot electron fluxes (the intense fluxes below ~10 eV in this regime are spacecraft photoelectrons), and the averaged OCB at ~13.3°. In some cases a further specific increase in I_m occurs in association with the OCB, indicative of strongly enhanced downward currents flowing on outermost closed field lines, examples of which are seen in Figures 4a and 4d, but not in all, such as Figure 4c and 4e. Such enhanced downward currents are an almost invariable feature of the southern current profiles, but are evident only intermittently in the north. The equatorward current then typically reaches peak positive values ~1–2 MA rad^{-1} at ~14°–16° colatitude, in agreement with the peak averaged profile in Figure 3b. The electron spectrograms show that this peak maps near the poleward boundary of the main hot (~100 eV to several keV) electron population, which according to our simple field model maps between ~14 and ~19 R_s in the equatorial outer magnetosphere.

Beyond the peak in I_m, a sharp reduction in value is then almost invariably observed over a ~1°–3° colatitude interval centered near ~15°–17°, indicative of a reversal to strong upward-directed field-aligned current, in overall agreement with Figure 3b. Examination of individual cases, however, shows that the form of the following field perturbations at larger colatitudes depends significantly on the values of both the northern and southern PPO phases. When both phases lie in the 180° range centered on 90°, both PPO systems are expected to be associated with positive azimuthal (leading) fields on subauroral field lines, corresponding to negative (poleward) I_m values, with upward field-aligned currents in the northern auroral region (Figures 1c–1h). A typical example is shown in Figure 4a (Rev 69), in which the I_m profile correspondingly falls to large negative values across the current layer, associated with a large upward current ~5 MA rad^{-1} in this case. I_m then returns to near-zero values across a secondary downward current layer of ~2 MA rad^{-1} centered near ~18° colatitude, before relaxing to smaller negative values across a weak adjacent upward current sheet ~0.5 MA rad^{-1} centered near ~19°. The latter current is co-located with the equatorward edge of the main hot electron region in the ELS spectrogram, mapping to ~8 R_s in the equatorial plane in our simple field model, although hot plasma injection signatures are present at larger colatitudes. (The high fluxes recorded across all electron energies at the largest colatitudes shown, striped in this case due to instrument scanning, result from penetrating energetic radiation belt particles and should be ignored.) The auroral region field-aligned currents between ~15° and ~19° in this case thus exhibit a four-sheet current profile as marked by the vertical dashed lines in the figure, that strongly resembles those observed in the southern hemisphere when upward-directed PPO currents are present (for southern PPO phases ~270°, see Figure 1g and Figure 4 of *Hunt et al.* [2014]), although the sheets are located a degree or two poleward of those in the south for reasons previously discussed. At larger colatitudes away from these current sheets the I_m values in Figure 4a then slowly increase to small positive values (negative azimuthal fields) as first the southern and then the northern PPO phases increase toward and across 180°.

Similarly, when both phases lie in the 180° range centered on 270°, both PPO systems are expected to be associated with negative azimuthal (lagging) fields on subauroral field lines, corresponding to positive (equatorward) I_m values, with downward field-aligned currents in the northern auroral region (Figures 1c–1h). An example is shown in Figure 4b (Rev 66), in which the I_m profile initially falls to near-zero values across an upward current layer of ~2 MA rad^{-1}, before returning to smaller positive (lagging field) values across a downward current layer ~1.5 MA rad^{-1} centered at ~16° colatitude. The profile then exhibits variable large positive values before returning to smaller positive values across a secondary upward current sheet centered near ~20°, again co-located with the inner boundary of the hot electron regime. This profile again strongly resembles the four-sheet profiles observed in the southern hemisphere for downward-directed PPO current (southern PPO phases ~90°, see Figure 1g and Figure 4 of *Hunt et al.* [2014]), as marked by the vertical dashed lines in the figure. We note in this case, however, that the poleward boundary of the enhanced downward current region at smallest colatitudes is clearly not co-located with the OCB as judged from the electron spectrogram, as is usually the case in the south. The boundary in the electron data in this case is at ~11.5° colatitude, while the downward current enhancement starts near ~13°. We also note that the positive I_m region between ~16° and ~20° colatitude has a double-peaked structure, also not seen in southern profiles, indicative of the presence of weaker central up-down field-aligned currents between the secondary downward and upward currents marked by the vertical dashed lines. At the largest colatitudes observed on this pass we see that the small positive I_m values decline toward zero and then become negative. The latter signature indicates the influence of the southern PPO phase on these values,

which we note is approaching ~90° at this time expected to be associated with increasing negative values, while the northern phase is approaching ~360° expected to be associated with weakening but still positive values.

In Figures 4c and 4d we show two cases in which the northern and southern PPO currents have opposite expected senses within the northern auroral region, with the northern phase lying in the 180° range centered on 90° and the southern phase lying in the 180° range centered on 270° in Figure 4c, and vice versa in Figure 4d. In the case shown in Figure 4c (Rev 68), the auroral-region profile appears as an attenuated version of that in Figure 4b, with no clear enhancement in the poleward downward current at the OCB, followed by a sharp upward current of ~1 MA rad^{-1} which reduces the I_m values to near zero, and then a resumption of weaker variable positive values at larger colatitudes indicative of an overall downward current followed by a secondary upward current. This sense of behavior thus follows expectations based on the southern PPO phase near ~270°, rather than the northern PPO phase near ~90°, thus indicating the presence of southern-phase currents in the northern auroral region. In the case shown in Figure 4d (Rev 80), a region of enhanced downward current is present on outer closed field lines, but after peaking and then falling near ~15° to weak negative values in the usual main upward current region, ~2 MA rad^{-1} in this case, I_m then remains at small negative values to large colatitudes. This behavior suggests the near cancellation of the usual currents in the larger colatitude regime from ~16° to ~20° spanning the main hot electron region, as seen in Figures 4a and 4b, with a southern PPO phase near 90° and northern PPO phase near 270°. However, the generally negative values suggest that the southern perturbations are again the larger of the two at these colatitudes.

In Figure 4e (Rev 91) we show a different case where we expect to observe small effects of the PPO-related currents, where the PPO phases are either ~0°/360° or 180° in the auroral region (see Figure 1), the former for the northern phase, and the latter for the southern phase in the case shown. The current profile indicates a slight steepening toward higher downward currents on outer closed field lines, before falling rapidly between ~16° and ~17.5° colatitude from peak positive to weaker negative values via an upward current of ~3 MA rad^{-1}. I_m then returns to small negative values via a sharp downward current layer ~1 MA rad^{-1} at ~18°, and remains at such values through the remainder of the hot electron regime and at larger colatitudes. The latter negative values are suggestive of dominance of the northern PPO system approaching ~90° phase in this case, rather than the southern system approaching ~270°. As may be expected, the nature of the auroral region current profile is similar in form to the mean current profile in Figure 3b, though of somewhat greater magnitude, taken to be an approximation to the form of the PPO-independent current. As in the southern hemisphere, in addition to the principal downward then upward currents, there is also indication of the presence of weaker secondary currents flowing at the equatorward edge of the upward current, a narrow sheet of downward current being evident in this case.

In addition to the more "regular" I_m profiles exemplified in Figures 4a–4e, four more unusual examples are also found within the northern data set, which have no clear counterpart within the southern data examined in *Hunt et al.* [2014]. One of these, observed on Rev 87, is shown in Figure 4f, the other three occurring under similar dual PPO phase conditions on Revs 72, 75, and 95. In these cases a patch of hot electrons is observed at high colatitudes, apparently "disconnected" from the usual hot electron regime at larger colatitudes, accompanied by a dip in the I_m profile to near zero and, in the present case, negative values. We use the word "apparently" here since it is unclear whether this feature represents a spatial or a temporal feature. Interpreted as a spatial feature, the I_m profile indicates the presence of an upward followed by a downward current region accompanying the crossing of an unusual outer layer of hot plasma. Interpreted as a temporal feature, the data indicate that the spacecraft entered a hot plasma region at unusually high latitudes in which an upward current was flowing, followed by a retreat of that regime away from the spacecraft either in latitude or LT, followed by a resumption of more usual conditions. The perturbations at larger colatitudes are then akin to those observed in Figure 4b under similar dual PPO phase conditions, and to those observed in attenuated form in Figure 4c.

Apart from these somewhat unusual profiles, this overview indicates more generally that while the current profiles in the northern hemisphere follow similar overall behavior to those observed in the south discussed previously by *Hunt et al.* [2014], they also show much less regularity in form compared with the PPO-dependent four-sheet structures usually found in the south. The clear latitudinal motion of the current layers with PPO phase that is present in the south is also absent in the north and is not clearly revealed either within the scatter of the limited data set by more detailed analysis of the current sheet positions in the manner of

section 5 of *Hunt et al.* [2014]. No such results will therefore be presented in this paper. This less regular behavior is undoubtedly linked to the additional finding that while the field perturbations in the northern polar region appear related to the northern PPO phase, those within the auroral region and at lower latitudes show dual influence of both northern and southern phases, which are essentially arbitrarily related over the data set as a whole. These data thus provide the first observational evidence for the existence of inter-hemispheric PPO-related currents proposed by *Southwood and Kivelson* [2007] (see also Figures 1d and 1g and related discussion in section 1). We note, however, that no clear evidence for the influence of the northern phase in ordering the southern data was found in *Hunt et al.* [2014]. In the following section we examine the issue of the presence of dual periodicities more quantitatively, not only for the northern, but also for the southern data.

4. Results

4.1. PPO-Related Azimuthal Fields at Small and Large Colatitudes

We begin by examining the field oscillations at small and large colatitudes away from the main current region, representing the overall effect of the PPO current system on open field lines and in the quasi-dipolar field region, respectively, in both the northern and southern hemispheres (see Figures 1c–1h). In view of the results of section 3.2, we plot the $B_{\varphi i}$ data in these two colatitude regimes versus both the northern and southern phases, $\Psi_{N,S}$, in the top row of Figure 5 for the northern hemisphere data mapped to the northern ionosphere, and in the bottom row for the southern hemisphere data mapped to the southern ionosphere (the latter as in *Hunt et al.* [2014]). Specifically, from the results in Figure 3 we choose the northern colatitude range $\theta_{iN} = 6°–11°$ for the polar region, and 20°–26° for the equatorward region (mapping to 3.8–6.6 R_s in the equatorial plane according to the field model in section 2.1), compared with ~14°–17.5° for the main current region. These polar and equatorial ranges are shown by the vertical dotted lines in Figure 3a. In the southern hemisphere we similarly use the ranges $\theta_{iS} = 6°–12°$ for the polar region, and 22.1°–28.8° for the equatorward region, shown by the vertical dotted lines in Figure 3c, the equatorward range being magnetically conjugate to the equatorward range in the northern hemisphere according to our field model. We note that the latter ranges are similar to, but slightly broader than the southern hemisphere ranges employed for similar purposes by *Hunt et al.* [2014] (see their Figure 5). We also note that both polar regions are expected to lie wholly on open field lines according to the average OCB locations determined by *Jinks et al.* [2014] (see Figure 3). The data from individual Revs are color-coded as in Figure 3.

From the discussion in section 1 we expect that in the equatorward region $B_{\varphi i}$ should vary as ~ sin $\Psi_{N,S}$, while in the polar region it should vary as ~ – sin $\Psi_{N,S}$, which visual inspection of Figure 5 shows is approximately the case for the phases in corresponding hemispheres. More quantitatively, we have fitted sinusoids to these data of the form

$$B_{\varphi i} = \langle B_{\varphi i} \rangle + B_{\varphi i 0} \sin\left(\Psi_{N,S} - \Delta\right), \tag{8}$$

obtained using a Levenberg-Marquardt least squares minimization algorithm [*Markwardt*, 2009], shown in Figure 5 by the black solid lines, with the mean value $\langle B_{\varphi i} \rangle$ being shown by the black dashed lines. The fit parameters together with the RMS deviation are shown in the upper left hand corner of each panel. The uncertainties in these parameters have been estimated using the "jackknife" statistical resampling method, in which one data set at a time is removed from the analysis and the fit parameters recomputed [see *Rohde et al.*, 2013, and references within]. In this case a data set has been defined as the data from a single Rev, thus resulting in 34 estimates of the fit parameters considering the 34 Revs included in the northern study. The estimated error in each parameter is given by a modified standard deviation $\sqrt{N-1}\sigma$, where N is the number of estimates (data sets or Revs) and σ the standard deviation of the fit parameter estimates [*Rohde et al.*, 2013]. For the phase angles Δ we employ the "circular standard deviation" of *Mardia and Jupp* [2000] [see *Andrews et al.*, 2011, equations (A1a) and (A3b)]. These uncertainties have been checked using a different statistical resampling method called the "bootstrap" method, in which the data sets (Revs) are randomly picked to form a new set of 34, with each Rev being allowed to be picked multiple times. The new set is then used in the fitting analysis, repeated N times to give N estimates of the fit parameters. The estimated uncertainty is the standard deviation of the fit parameter. It was found that bootstrap values for $N \approx 1000$ generally produced uncertainty estimates very similar to those obtained from the jackknife method. The latter method was chosen for this study, however, due to its smaller computation requirements.

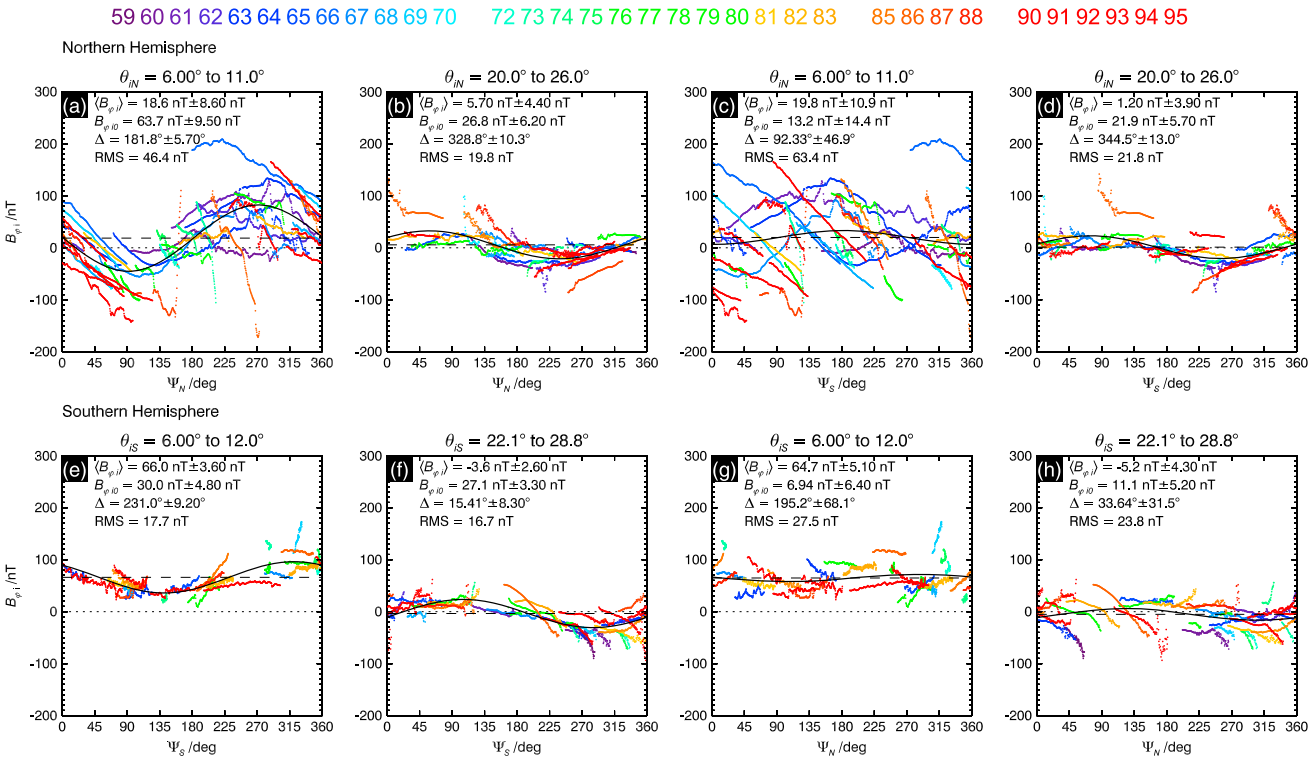

Figure 5. (a–h) Plots showing the variation of the mapped northern and southern ionospheric azimuthal field $B_{\varphi i}$ (nT) with northern and southern PPO phases $\Psi_{N,S}$ (deg). The northern hemisphere data have been mapped to the northern ionosphere, and the southern data to the southern. Figures 5a and 5c show northern polar data poleward of the auroral current sheets (6°–11° northern colatitude) plotted versus northern and southern phases, respectively, while Figures 5b and 5d correspondingly show the northern equatorial data equatorward of the current sheets (20°–26° colatitude). Similarly, Figures 5e and 5g show southern polar data (6°–12° southern colatitude) plotted versus northern and southern phases, respectively, while Figures 5f and 5h correspondingly show the southern equatorial data (22.1°–28.8° colatitude conjugate to the northern equatorial region). The data from each Rev are color coded as shown at the top of the plot. The black solid lines show sinusoidal fits to these data as described in section 4.1 (equation (8)), with the fit parameters given in each panel together with the RMS deviation of the data from the fitted line. The black dashed line shows the mean value.

Turning now to the results, we see in Figure 5a that the amplitude of the northern polar oscillation is ~64 ± 10 nT, thus accounting for much for the variation about the mean in the corresponding region in Figure 3a, while the phase Δ is ~182° ± 6°, very close to the expected value of 180° based on *Andrews et al.*'s [2012] model. The uncertainty estimates indicate that both these parameters are well determined. The mean value is ~19 ± 9 nT, consistent with the mean values in Figure 3a, while the RMS deviation is ~46 nT, to which the variation of ~70 nT in the mean profile over the chosen polar region in Figure 3a must make a significant contribution. For the equatorial data in Figure 5b the amplitude is smaller ~27 ± 6 nT, while the phase is ~329° ± 10°, again well determined. The latter value is equivalent to -31° ± 10° (modulo 360°), which is modestly but significantly "earlier" compared with the zero value expected on the basis of *Andrews et al.*'s [2012] model. Compared with the results in Figure 5a, this value implies that the oscillations in the polar region "lag" the equatorial phase by ~33° ± 12°. A similar phenomenon was reported in southern data by *Hunt et al.* [2014], who, allowing for the expected ~180° switch between the two regions as above, found that the southern hemisphere polar oscillations lagged in phase by ~47° relative to the southern equatorial oscillations.

Similar analysis of the southern hemisphere data relative to Ψ_S is shown in Figures 5e and 5f. Here the equatorial amplitude is ~27 ± 3 nT similar to the equatorial northern oscillation amplitude in the northern hemisphere in Figure 5b, with a phase of ~15° ± 8° which is slightly but significantly larger than the expected value of zero. For the southern polar data, however, the amplitude is ~30 ± 5 nT, approximately half that in the northern polar region, with a phase of ~231° ± 9°, significantly "later" compared to the expected phase of ~180°. Again, allowing for the expected 180° phase shift between the two regions, the polar oscillations in the south thus lag the equatorial oscillations by ~36° ± 12°. Thus, very similar phase lags ~35° are found between the equatorial and polar regions both north and south, consistent within uncertainties with the

slightly larger southern hemisphere value ~47° reported previously by *Hunt et al*. [2014]. This analysis also shows that for this interval the *Andrews et al*. [2012] phase model best reflects the polar data in the northern hemisphere but the equatorial data in the southern hemisphere, presumably reflecting the relative influence of the equatorial and polar data employed in their analysis.

Given the results in section 3.2, we also examine whether oscillations with the southern PPO period can be detected in the northern regions, and vice versa. Results for the northern hemisphere are shown in Figures 5c and 5d, where the northern hemisphere polar and equatorial data, respectively, are plotted versus the southern phase Ψ_S. In the polar region neither the data nor the sinusoidal fit show any evident modulation by the southern phase, with the fitted amplitude ~13 ± 14 nT consistent with zero. In the equatorial region, however, clear southern modulation is evident with an amplitude ~22 ± 6 nT, only slightly smaller than the northern oscillation in Figure 5b, and a phase of ~345° ± 13°, essentially consistent with the expected value of zero. The latter phase is modestly ~30° ± 15° away from that determined from the southern hemisphere equatorial data in Figure 5f. These results thus confirm the conclusions in section 3.2, that while southern oscillations are not discernible in the northern polar region, a clear effect is present in the northern equatorial region. The amplitude is comparable with but somewhat lower than that determined from the southern equatorial data and is also comparable with but somewhat lower than the northern oscillations in the northern equatorial region. The variation of oscillation amplitude with latitude along the equatorial field lines will be examined in greater detail in section 4.4.

In Figures 5g and 5h we similarly show the polar and equatorial southern hemisphere data plotted versus northern phase Ψ_N. In this case there is again no discernible effect in the polar region, with an amplitude of ~7 ± 6 nT again consistent with zero. In the equatorial region the amplitude is found to be ~11 ± 5 nT, less than half that in the northern hemisphere in Figure 5b and less than that of the southern oscillations in this region by a factor of ~2.5, with a phase ~34° ± 31° with a large uncertainty which is ~66° ± 33° away from the northern phase in Figure 5b. This rather marginal result will again be further examined in section 4.4.

4.2. PPO Dependence of Northern Current Colatitude Profiles

We now examine the PPO phase dependence of the northern colatitude profiles of the meridional ionospheric current per radian of azimuth I_m, by dividing the northern hemisphere data from all the Revs in the study into fixed ranges of $\Psi_{N,S}$. We recall from section 2.2 that I_m is derived from the corrected azimuthal field values using equation (5), is thus opposite in sign to B_φ and positive directed toward the equator, and that it can be used under appropriate conditions to directly discuss the field aligned currents that are flowing. *Hunt et al*. [2014] (their section 4.2) performed an equivalent analysis for the southern data by dividing it into eight nonoverlapping 45° sectors of Ψ_S, centered on 0°, 45°, 90°, and so on. Here, however, in view of the results in sections 3.2 and 4.1, which imply that the northern equatorial data depend both on Ψ_N and Ψ_S, we instead divide the data into nonoverlapping 90° sectors of both Ψ_N and Ψ_S, each centered on 0°, 90°, 180°, and 270°.

The results are shown in Figure 6 in a Ψ_N by Ψ_S grid, where Ψ_N increases from top to bottom and Ψ_S from left to right. Thus, row 1 (Figures 6a–6d) contains all the data for $\Psi_{N,S} = 0° \pm 45°$, subdivided into four 90° sectors of Ψ_S, while column 1 (Figures 6a, 6e, 6i, and 6m) contains all the data for $\Psi_S = 0° \pm 45°$, subdivided into four 90° sectors of Ψ_N, and so on for the other rows and columns. The data from individual Revs are color-coded as in previous figures, while the black solid circles joined by straight lines show values averaged as in Figure 3 described in section 3.1. While the data coverage is generally reasonably good within each of these $\Psi_{N,S}$ sectors, thus justifying the choice of sector size, there are some notable gaps, for example, the main current region in Figure 6p.

Given the approximate dependency of the ionospheric current on $\Psi_{N,S}$ as $+\sin\Psi_{N,S}$ in the polar region and $\Psi_{N,S}$ in the equatorial (opposite to $B_{\varphi i}$), and neglecting the ~30° phase offsets found in section 4.1 as modest compared with the 90° sector size used here, we note that the sectors centered on $\Psi_{N,S} = 0°$ or 180° should show minimal effects due to the corresponding PPO current system, while sectors centered on $\Psi_{N,S} = 90°$ and 270° should show maximal effects of opposite sign. Thus, the data in columns 1 and 3 should show how the northern current profile varies with northern phase in the approximate absence of southern PPO effects, while rows 1 and 3 should show the equivalent variation of the northern current profile with southern phase in the approximate absence of northern PPO effects. The four remaining sectors not included in either

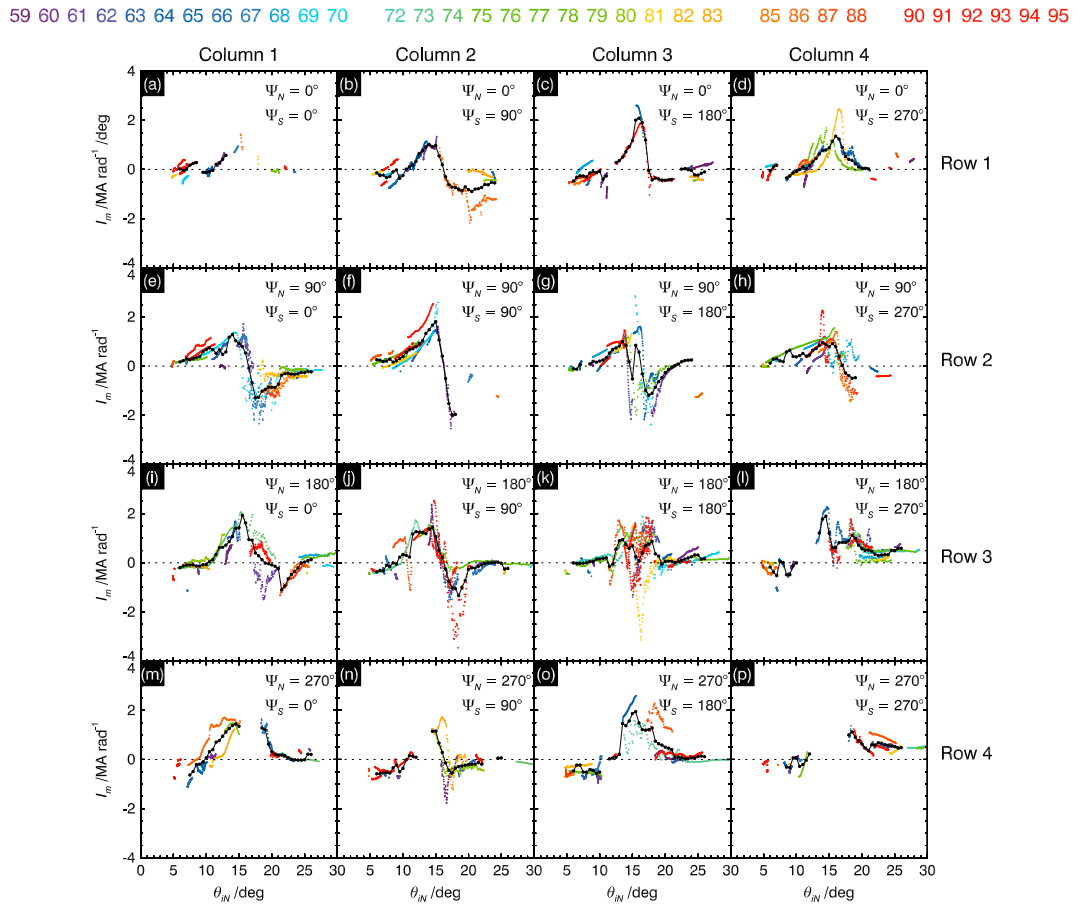

Figure 6. (a–p) Plots showing northern ionospheric colatitude (θ_{iN} (deg)) profiles of the meridional ionospheric current per radian of azimuth I_m (MA rad^{-1}) subdivided into sixteen non overlapping 90° sectors of northern and southern PPO phases Ψ_N and Ψ_S (deg). The center phase values are shown in the top right corner of each panel, with Ψ_N increasing from top to bottom, and Ψ_S increasing from left to right. The data for each Rev are color coded as shown at the top of the figure, while black circles joined by black lines show weighted averages in overlapping 1° bins of colatitude, evaluated every 0.5°, as for Figure 3, where the data coverage is near continuous.

of these columns and rows (Figures 6f, 6h, 6n, and 6p) then show cases where the two PPO systems either add in phase ($\Psi_{N,S}$ both 90° or both 270°), or partially cancel in antiphase (one 90° and the other 270°).

We first examine the data that lie both in columns 1 and 3 and rows 1 and 3 (Figures 6a, 6c, 6i, and 6k), for which both northern and southern PPO effects should be minimal, $\Psi_{N,S}$ both centered on 0° or 180°, such that the profiles should approximate the PPO-independent current profile in the northern hemisphere. Similar profiles are seen in each case, with small currents in the most poleward region which increase quickly with colatitude beyond ~11°, indicative of a downward current layer which is initiated generally on open field lines (according to the *Jinks et al.* [2014] averaged northern OCB at ~13.3°). The ionospheric current then peaks at ~1–2 MA rad^{-1} at ~16° colatitude (mapping to ~14 R_s in the equatorial plane similar to *Hunt et al.* [2014]), and then falls rapidly to small values by ~18°–19° (mapping to ~9–7.5 R_s in the equatorial plane), indicative of an upward current layer, then remaining small to large colatitudes. We note, however, the strongly scattered data with a double-peaked averaged profile in Figure 6k. The overall profiles resemble less smoothed versions of the mean I_m profile in Figure 3b, with small or lagging fields (positive I_m) essentially throughout, and an overall current in the system that is close to zero, with no net change in I_m over the colatitude range observed.

By comparison, the two sectors centered on $\Psi_N = 90°$ in columns 1 and 3 (Figures 6e and 6g) both show enhanced positive values in the polar region and enhanced negative (leading field) values in the equatorial region, before increasing sharply toward zero by ~21° colatitude (mapping to ~5.8 R_s). These profiles thus

indicate the additional presence of an upward current that is comparable in magnitude to the upward current of the PPO-independent system and is approximately collocated with the latter. At the equatorward edge of this current, the return of I_m to near zero values is also indicative of a smaller downward current which reduces the magnitude of the field perturbations in the inner region. Similarly, the two sectors centered on $\Psi_N = 270°$ in columns 1 and 3 (Figures 6m and 6o) show enhanced negative values in the polar region compared with the profiles for $\Psi_{N,S} = 0°$ and 180° and enhanced positive values in the equatorward region which again fall to near-zero values at ~20°–21°. This indicates the presence of a downward current superposed on the PPO-independent current region together with a smaller upward current at larger colatitudes. These systems will be separated and examined in more detail in section 4.3.

Similar examination of rows 1 and 3 gives two independent determinations of the effects on the current profiles associated with the southern PPO phase, with the effects of the northern PPO signal minimized (Figures 6b, 6d, 6j, and 6l). While there is no obvious effect of the southern phase in the polar region, it can be seen that a negative perturbation is present at larger colatitudes for Ψ_S centered on 90° (Figures 6b and 6j), indicative of an upward current superposed on the equatorward part of the PPO-independent current, while a positive perturbation is seen in the same region for Ψ_S centered on 270° (Figures 6d and 6l), indicative of a downward current superposed on the PPO-independent current. These currents will also be examined in more detail in section 4.3.

The remaining four phase sectors in Figure 6 are the cases where both northern and southern PPO effects should have near maximal values, both 90° or both 270°, thus in phase with each other, or where one phase is 90° and the other 270°, thus in antiphase. The case where both phases are centered on 90° is shown in Figure 6f, which has the largest negative (leading field) current at large colatitudes within this data set, due to the superposition of two upward PPO-related currents. The other in-phase case, with both phases centered at 270°, is shown in Figure 6p, which unfortunately has a large gap with no data in the main current region. However, it does show negative values at small colatitudes and positive values at large colatitudes, as then expected from a superposed net downward current. For the two cases of antiphase, Figures 6h and 6n, the sign of the polar field perturbations agree with expectations based on Ψ_N, positive at 90° and negative at 270°, while the main current region shows significant data scatter, with the current in the equatorial region near zero at colatitudes greater than ~18°.

4.3. Subcorotation and PPO-Dependent Current Profiles

We now combine the data in Figure 6 in various ways to make estimates of the PPO-independent (subcorotation) and the PPO-dependent current profiles and thus also estimates of the associated field-aligned currents. We also compare these profiles with those derived from the southern hemisphere data investigated by *Hunt et al.* [2014]. We begin by considering the PPO-independent current profile, which can be determined by combining the data centered on $\Psi_{N,S} = 0°$ and 180° (Figures 6a, 6c, 6i, and 6k), for which the effects of both northern and southern PPO currents should be minimized. The averaged profile is shown in Figure 7a (the average being determined as in Figure 3), showing small negative values at smallest colatitudes ~5°–10° similar to Figure 3b, then increasing steadily between ~11° and ~13.5° colatitude (near the averaged northern OCB of *Jinks et al.* [2014] shown by the vertical dashed line in the figure), indicating a downward current of ~1 MA rad^{-1} in this region with an ionospheric current density of ~25 nA m^{-2}. Only moderate variations in the average value then occur between ~14° and ~17°, followed by a decrease to near-zero values over ~17° to ~19°, showing an essentially equal and opposite upward current flowing in this region of ~1 MA rad^{-1} again with an ionospheric current density of ~25 nA m^{-2}. We note, however, that there is strong variability of the data in the upward current region from Rev to Rev, such that this profile very much represents an averaged view.

Now we consider the PPO-related current profile due to the northern system, for which we choose data from Figure 6 that maximize the effect of the northern PPO while minimizing the effect of the southern. That is, we select the sectors with $\Psi_N = 90°$ and 270° for which $\Psi_S = 0°$ and 180° (Figures 6e, 6g, 6m, and 6o). We then combine the $\Psi_S = 0°$ and 180° data to give the best estimate of the profiles for given Ψ_N in the approximate absence of southern PPO effects, and thus determine the mean profiles for $\Psi_N = 90°$ and 270°. Exploiting the expected $m = 1$ symmetry of the PPO system with respect to PPO phase as in *Hunt et al.* [2014], we then subtract the $\Psi_N = 90°$ profile from the 270° profile (or vice versa) and divide by two to extract the northern PPO-related current that is superposed on the PPO-independent current, the latter being eliminated by

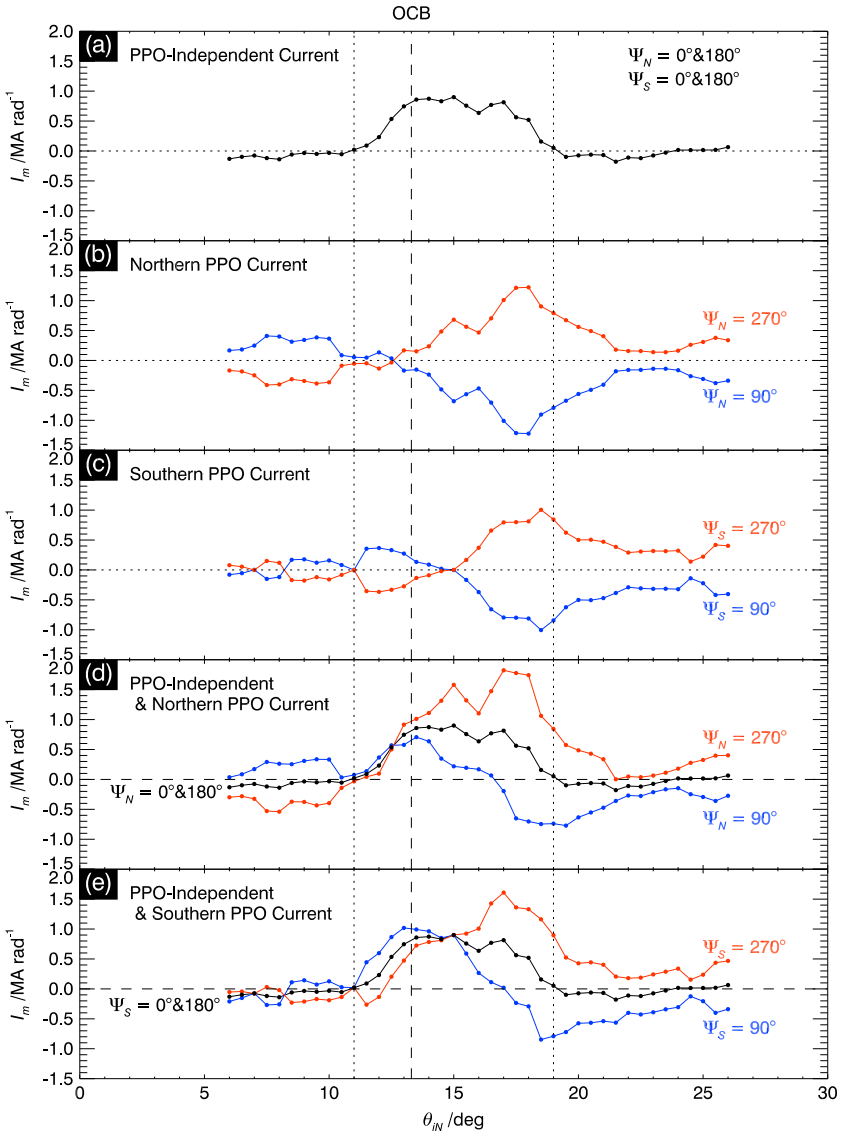

Figure 7. Northern colatitude profiles of the meridional ionospheric current I_m (MA rad^{-1}) associated with (a) the PPO-independent (subcorotation) system, (b) the northern-period PPO system where the blue data corresponds to $\Psi_N = 90°$ and the red to $\Psi_N = 270°$, and (c) the southern PPO system where the blue data corresponds to $\Psi_S = 90°$ and the red to $\Psi_S = 270°$. These were derived using data from appropriate sectors in Figure 6, as described in section 4.3. The vertical dotted lines indicate the main region of equatorward current and lagging azimuthal field in the PPO-independent system between ~11° and ~19°. The vertical dashed line shows the position of the averaged northern OCB of *Jinks et al.* [2014] at 13.3°. (d) Synthesized profiles that add the northern PPO profiles from Figure 7b to the PPO-independent profile in Figure 7a, to show the combined profiles for $\Psi_N = 90°$ (blue), $\Psi_N = 0°$ and 180° (black) (just Figure 7a), and $\Psi_N = 270°$ (red). No contribution is included from the southern system, corresponding to $\Psi_S = 0°$ and 180° throughout. (e) Synthesized profiles that add the southern PPO profiles from Figure 7c to the PPO-independent profile in Figure 7a, to show the combined profiles for $\Psi_S = 90°$ (blue), $\Psi_S = 0°$ and 180° (black) (again just Figure 7a), and $\Psi_S = 270°$ (red). No contribution is included from the northern system, corresponding to $\Psi_N = 0°$ and 180° throughout.

the subtraction. The results are shown in Figure 7b where the equal and opposite blue and red profiles correspond to $\Psi_N = 90°$ and 270°, respectively. Vertical dotted lines extended from Figure 7a indicate the main region of equatorward-directed current and lagging field associated with the PPO-independent system, located between ~11° and ~19°. Essentially within this region the $\Psi_N = 90°$ profile undergoes a strong decrease indicative of an upward current of ~1.5 MA rad^{-1}, while the equal and opposite $\Psi_N = 270°$ profile undergoes a strong increase indicative of a downward current of the same magnitude. The implied overall ionospheric field-aligned current density is ~20 nA m^{-2}. We note that the overall current gradient in this

region is comparable to the ~0.3 MA rad^{-1} limit described in section 2.2, 10 times that which might occur in the absence of field-aligned currents. These are the PPO-related field-aligned currents that separate the oppositely-directed current and azimuthal field perturbations in the polar (~5°–10°) and equatorial (beyond ~18°) regions, as examined in section 4.1 and Figure 5. We note that the switch in sign between perturbations of opposite senses occurs at ~12.5° colatitude, poleward of but close to the northern averaged OCB (~13.3°). At larger colatitudes beyond ~18°, however, the current drops rapidly to small values of the same sign beyond ~21.5°. Again, the current gradient is significant in the above terms, indicating the presence of field-aligned currents of opposite sense, downward for $\Psi_N = 90°$ and upward for 270°, of magnitude ~1 MA rad^{-1}, which reduce the field perturbations to lower magnitudes in the large colatitude regime. This current layer maps between ~9 and ~6 R_s in the equatorial plane and has an associated ionospheric field-aligned current density of ~15 nA m^{-2}. We note that a similar feature of ~0.4 MA rad^{-1} magnitude was found previously in the southern PPO current profile by *Hunt et al.* [2014] (see their Figures 9 and 15), but in this case the gradient of the current did not meet the above criterion for the unambiguous presence of field-aligned current, such that it was not described in those terms.

The current profile associated with the southern PPO system in the northern hemisphere is determined in a similar way by combining the data sectors in Figure 6 that maximize the southern PPO effects while minimizing the northern PPO effects. Thus, we employ the data centered on $\Psi_S = 90°$ and 270° with $\Psi_N = 0°$ and 180° (Figures 6b, 6d, 6j, and 6l), combine and average the latter data for given Ψ_S, and then subtract these profiles and divide by 2. The results are shown in Figure 7c, where the blue profile corresponds to $\Psi_S = 90°$ and the red to $\Psi_S = 270°$. As for the northern system in Figure 7b, the main currents flow in the region between the dashed vertical lines, implying an upward current of ~1.25 MA rad^{-1} for $\Psi_S = 90°$ and a downward current of the same magnitude for $\Psi_S = 270°$, modestly smaller than the corresponding current for the northern PPO system indicated above. Again, the gradient is significant, indicative of an ionospheric current density of ~13.5 nA m^{-2}. Unlike the northern system, however, poleward of this region the current falls to small values of variable sign, consistent with the null result in Figure 5c discussed in section 4.1, indicative of the presence of an oppositely-directed field-aligned current of ~0.35 MA rad^{-1} near ~11.5° colatitude. Equatorward of the main layer the current again falls sharply to smaller values of the same sign across ~18.5° to ~22.0° (~9–5 R_s in the equatorial plane), indicative of a layer of oppositely directed current of ~0.75 MA rad^{-1} with an ionospheric current density of ~11 nA m^{-2}. Beyond this current layer the I_m values remain near constant at least to ~26° at values comparable with those for the northern PPO system in Figure 7b.

Using these results we can synthesize northern current profiles that are not observed directly, such as those corresponding to a fixed northern or southern PPO phase in the absence of the other PPO system. In Figure 7d, for example, we show the modulation of the northern current profile by the northern PPO system in the absence of southern effects. Specifically, we combine the PPO-independent profile in Figure 7a with the northern PPO profiles for $\Psi_N = 90°$ (blue) and 270° (red) in Figure 7b, but do not include a contribution from the southern PPO system, thus corresponding to $\Psi_S = 0°$ or 180°. We also show the PPO-independent profile itself (black), corresponding to both $\Psi_N = 0°$ or 180° and $\Psi_S = 0°$ or 180°. The correspondence of these profiles for the northern system in the northern hemisphere with the results of *Hunt et al.* [2014] for the southern system in the southern hemisphere is clear (see, e.g., their Figures 7 and 11). For $\Psi_N = 90°$, the counterpart of $\Psi_S = 270°$ in the southern hemisphere (see Figure 1), we see from the pole to the equator (a) a downward current layer of ~0.5 MA rad^{-1} between ~10.5° and ~13.5°, just spanning the averaged OCB at ~13.3°, (b) an upward current layer ~1.5 MA rad^{-1} between ~13.5°and ~18° spanning the UV auroral oval in Figure 2c with "leading" fields (poleward-directed current) in the equatorward portion, and (c) a further downward current ~0.75 MA rad^{-1} between ~19.5° and ~24°. This three-layer structure is therefore very similar to that observed for $\Psi_S = 270°$ in the south, although a small secondary upward current layer is also present at largest southern colatitudes which is either not present or not resolved here. Similarly, for $\Psi_N = 270°$, the counterpart of $\Psi_S = 90°$ in the southern hemisphere, we see from the pole to the equator (a) a larger downward current layer of ~2 MA rad^{-1} between ~10° and ~15°, (b) a much smaller upward current layer ~0.5 MA rad^{-1} between ~15° and ~16°, (c) a small further downward current ~0.75 MA rad^{-1} between ~16° and ~17°, and (d) a large downward current ~1.75 MA rad^{-1} between ~17° and ~21.5°. This four-layer structure is very similar in form to that observed for $\Psi_S = 90°$ in the south, overall representing a broad region of equatorward current associated with lagging fields with a "V-shaped" dip in the current magnitude near its the center.

In Figure 7e we similarly show profiles corresponding to fixed values of the southern PPO phase, $\Psi_S = 0°$ or 180° (black), $\Psi_S = 90°$ (blue), and 270° (red) from Figures 7a and 7c, with no contribution from the northern PPO system, corresponding to $\Psi_N = 0°$ or 180°. A similar modulation of the currents in the equatorward region is evident in this case, though with no clear PPO-related modulation at poleward-most latitudes. The profile for $\Psi_S = 90°$ is again of similar three-layer down-up-down form as that for $\Psi_N = 90°$ in Figure 7d, while in the profile for $\Psi_S = 270°$ the expected dip in the center of the equatorward current region is either absent or unresolved, leading to a two-sheet down-up structure with a near-plateau region between ~14° and ~16°.

We can also use the results in Figures 7a–7c to synthesize profiles corresponding to other cases, such as where the PPO systems are in phase or in antiphase. In this context it may be noted that the three sets of results shown in Figures 7a–7c were each derived using a different set of four of the sixteen independent 90° × 90° PPO phase data sets in Figure 6, thus corresponding to 12 of the 16 sets. The four remaining data sets not employed so far correspond to cases in which significant effects of both PPO systems should be present, either in phase with each other with $\Psi_N = \Psi_S = 90°$ (Figure 6f) or $\Psi_N = \Psi_S = 270°$ (Figure 6p), or in antiphase with each other, with either $\Psi_N = 90°$ and $\Psi_S = 270°$ (Figure 6h) or vice versa (Figure 6n). It is then of interest to see how appropriate combinations of the independently determined profiles in Figure 7 compare with these data, with results shown in Figure 8. Figure 8a shows the summed northern and southern PPO current profiles from Figures 7b and 7c for $\Psi_N = \Psi_S = 90°$ (blue) and $\Psi_N = \Psi_S = 270°$ (red), while the black profile shows the PPO-independent current profile from Figure 7a. The main poleward PPO currents sum to ~2.5 MA rad^{-1} under these conditions, with oppositely directed currents of ~1.5 MA rad^{-1} flowing in the equatorward region. Adding the combined current profile for $\Psi_N = \Psi_S = 90°$ to the PPO-independent profile yields the black profile shown in Figure 8b, which is superposed on the corresponding independent data from Figure 6f. The overall agreement is quite good, although the central upward current layer is somewhat reduced in magnitude and smoothed compared to the data. Overall, a downward current of ~1 MA rad^{-1} flows in the poleward region to ~14°, followed by an upward current of ~3–4 MA rad^{-1} flowing between ~14° and ~18°, and then a second downward current of ~1.5 MA rad^{-1} flowing between ~18° and ~22°. Similarly, combining the profile for $\Psi_N = \Psi_S = 270°$ in Figure 8a with the PPO-independent current profile yields the black profile in Figure 8c, which we compare with the corresponding data from Figure 6p. As mentioned in section 4.2, this data set unfortunately has a large gap in coverage in the main current region, but there is good agreement with the limited data at small and large colatitudes. Our synthesized profile thus provides an estimate of the currents in this case, corresponding to a region of downward current of ~3 MA rad^{-1} flowing between ~12° and ~18°, with a small dip near its center at ~15.5°, followed by a smaller upward current of ~2 MA rad^{-1} flowing between ~18° and ~21°.

Figure 8d shows the opposite case where the two PPO systems in Figures 7b and 7c are in antiphase, where the blue profile shows the case for $\Psi_N = 90°$ and $\Psi_S = 270°$, and the red for $\Psi_N = 270°$ and $\Psi_S = 90°$. Again, the black profile is the PPO-independent profile. Since the two PPO current profiles in Figures 7b and 7c are comparable in magnitude and essentially co-located, when combined in this way they cancel to a first approximation, but since the northern system is slightly stronger than the southern, the net current follows the northern system polarity, with opposite currents of ~0.75 MA rad^{-1} flowing in the poleward part of the region at ~10°–15°, and ~0.5 MA rad^{-1} at larger colatitudes at ~15°–18.5°. The PPO-independent current profile is then modestly larger compared with the PPO-related currents, opposite to the case when the two PPO systems are in phase. Combining the $\Psi_N = 90°$ and $\Psi_S = 270°$ (blue) profile with the PPO-independent current profile yields the black profile in Figure 8e, which we show with the corresponding data from Figure 6h. The synthesized profile remains small, generally positive, and variable over the colatitude range ~6° to 19°, in rough agreement with the generally positive and scattered data. For the opposite case with $\Psi_N = 270°$ and $\Psi_S = 90°$, the combined current yields the black profile in Figure 8f, similar in form but slightly enhanced compared with the PPO-independent profile alone, which is shown together with the corresponding data from Figure 6n. The synthesized profile has a downward current of ~2 MA rad^{-1} flowing at ~10°–15° colatitude, followed by a modestly weaker upward current of ~1.5 MA rad^{-1} between ~15° and 19°. The agreement with the data is again reasonable, although the model does not reproduce the sharp negative current features observed in the data at ~16°–17°.

We now compare these results derived from northern hemisphere data with those from the southern hemisphere on the same Revs as determined by *Hunt et al.* [2014]. We first consider the PPO-independent currents, and in Figure 9a compare the mean northern current profile in Figure 7a (black circles and solid lines) with

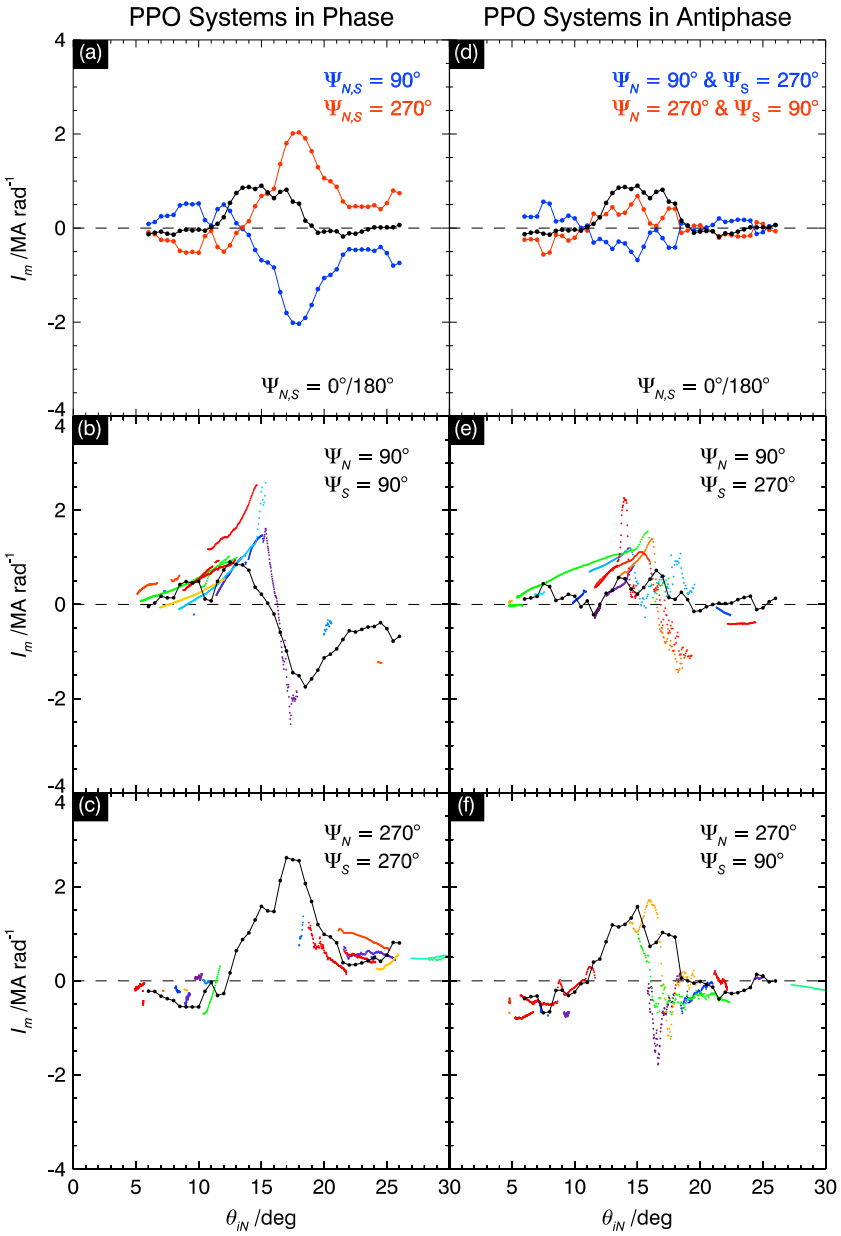

Figure 8. (a–f) Plots showing northern colatitude profiles of the meridional ionospheric current I_m (MA rad^{-1}) for cases in which the northern and southern PPO systems are either in phase or in antiphase, synthesized from the profiles in Figure 7. Figure 8a shows the PPO-independent current profile from Figure 7a (black) together with the summed northern and southern PPO system profiles for $\Psi_N = \Psi_S = 90°$ (blue) and $\Psi_N = \Psi_S = 270°$ (red) from Figures 7b and 7c, corresponding to times when the two PPO systems are in phase. In Figure 8b the black and blue profiles are added and compared with the corresponding independent data in Figure 6f, while in Figure 8c the black and red profiles are added and compared with the corresponding independent data in Figure 6p. Figure 8d again shows the PPO-independent current profile (black), together with the summed northern and southern PPO system profiles for $\Psi_N = 90°$ and $\Psi_S = 270°$ (blue), and $\Psi_N = 270°$ and $\Psi_S = 90°$ (red), corresponding to times when the two PPO systems are in antiphase. In Figure 8e the black and blue profiles are added and compared with the corresponding independent data in Figure 6h, while in Figure 8f the black and red profiles are added and compared with the corresponding independent data in Figure 6n.

that determined from a similar analysis of the southern data (black crosses and dotted lines), specifically using data for $\Psi_S = 0°$ and 180° (± 45°). Since the results discussed above show that the northern PPO effect is much smaller than the southern PPO effect in the southern hemisphere, we do not limit the Ψ_N values used in this case. This method is somewhat different to that employed by *Hunt et al.* [2014] (see their

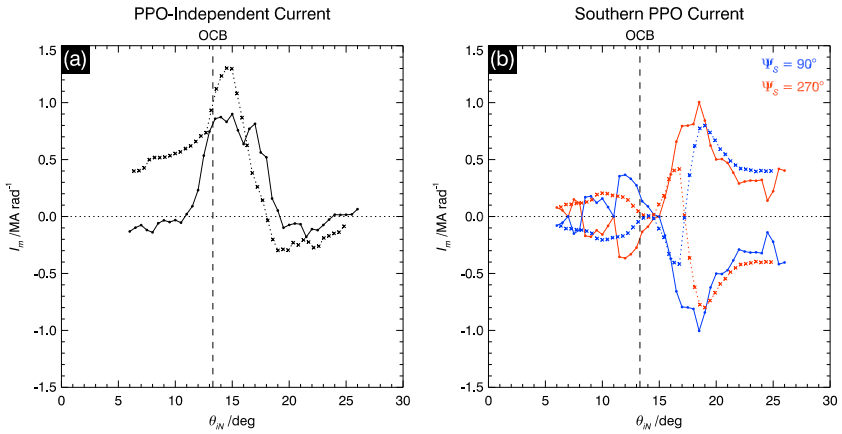

Figure 9. (a and b) Comparison between northern ionospheric meridional current profiles and those mapped along model field lines from the southern hemisphere. Figure 9a shows the northern and southern PPO-independent current profiles, where the black circles and solid lines show the northern hemisphere profile from Figure 7a, while the black crosses and dotted lines show the mapped southern hemisphere profile, determined from southern hemisphere data for $\Psi_S = 0°$ and 180° (±45°) irrespective of Ψ_N. Figure 9b compares the southern PPO-related current profile in the northern hemisphere, blue dots and solid lines for $\Psi_S = 90°$ and red dots and solid lines for $\Psi_S = 270°$, from Figure 7c, with the southern hemisphere southern PPO-related current profile mapped along field lines into the northern hemisphere, blue crosses and dotted lines for $\Psi_S = 90°$ and red crosses and dotted lines for $\Psi_S = 270°$. The vertical dashed lines in each panel show the position of the averaged northern OCB of *Jinks et al.* [2014].

sections 4.3 and 4.4), but produces a profile similar to Figure 9a in that paper, and to the overall average shown here in Figure 3d. The southern profile is then mapped along model field lines into the northern hemisphere for purposes of direct comparison with the northern PPO-independent profile. As shown in the Appendix A, for the same plasma subcorotation angular velocity on a given flux shell, and the same effective Pedersen conductivity, I_m is expected to be closely similar in the northern and southern hemispheres, such that a direct comparison is appropriate. It can be seen that in the region of closed lines ($\theta_{iN} > 13.3°$ according to *Jinks et al.* [2014], shown by the vertical dashed lines in Figure 9), the profiles are very similar as expected, but with the current in the southern hemisphere peaking at somewhat larger values than in the north, indicative of a modestly higher Pedersen conductivity in the southern hemisphere than in the northern. At smaller colatitudes, however, generally on open field lines, the profiles are clearly different, with the mapped southern profile falling slowly to lower positive values, while the northern profile falls sharply to near-zero and small negative values for colatitudes smaller than ~11°. This difference likely reflects the seasonal difference in the polar ionospheric Pedersen conductivity between the north and south under prevernal equinox conditions, with the northern spin and magnetic axis tilted away from the Sun by between 8° and 4° over the data interval, combined, possibly, with consequent differences in the open field plasma angular velocity.

In Figure 9b we similarly compare the southern PPO-related current in the northern hemisphere for $\Psi_S = 90°$ (blue circles and solid lines) and $\Psi_S = 270°$ (red circles and solid lines) from Figure 7c, with the corresponding profiles mapped from the southern hemisphere for $\Psi_S = 90°$ (blue crosses and dotted lines) and for $\Psi_S = 270°$ (red crosses and dotted lines). The southern hemisphere southern PPO profile has been calculated here by similarly averaging the profiles for $\Psi_S = 90°$ and $\Psi_S = 270°$ (irrespective of Ψ_N), subtracting and dividing by two. It can be seen that the main PPO currents are comparable in magnitude in the two hemispheres, ~1.25 MA rad^{-1}, but extend over a significantly larger colatitude range in the northern hemisphere, ~12° to ~18.5°, than in the southern, ~17° to ~19° as mapped (~18.5° to ~21° in the southern hemisphere itself). Equatorward of the main current region (colatitudes greater than ~18.5°), however, the mapped southern profile shows a smaller and less steep decline with increasing colatitude, as mentioned above, such that the values in the southern hemisphere remain modestly larger than those in the northern hemisphere to the limit of the joint data available, consistent with the results in Figures 5f and 5d. These results thus indicate the presence of a somewhat more complex PPO-related current system in the outer part of the

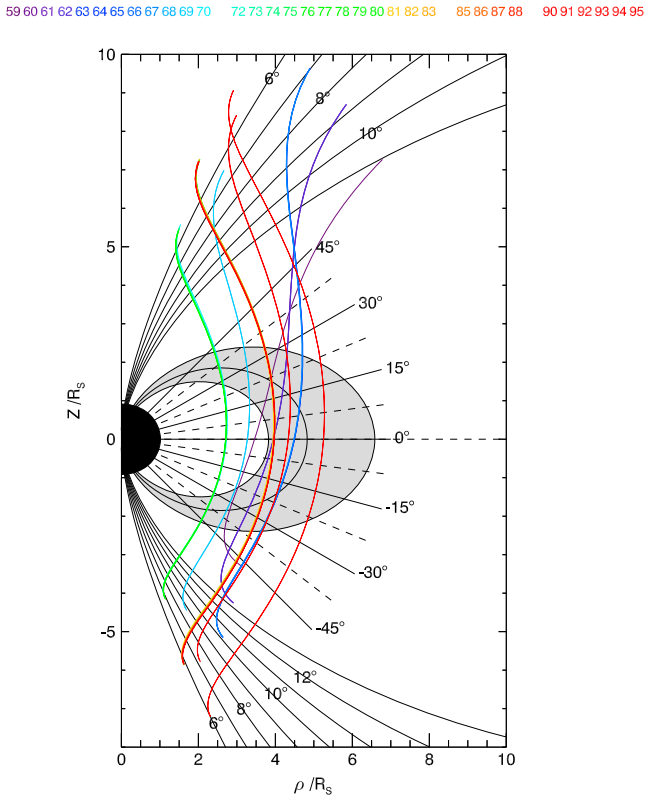

Figure 10. Plot of model magnetic field lines and the periapsis sections of the Cassini trajectories for Revs 59–95 mapped into a meridian plane in cylindrical (ρ,z) coordinates. The color-coding of the trajectories is shown at the top of the plot and is the same as in previous figures. The gray shaded flux shell is that used to investigate the latitudinal variation of the field oscillations equatorward of the main field-aligned current region in section 4.4 with results shown in Figure 11 and maps from 20° to 26° colatitude in the northern ionosphere to 22.1° to 28.8° in the southern. The radial lines show the overlapping 15° intervals of latitude λ (deg) used in this study, centered between ±37.5°. In the polar regions model field lines are shown plotted at 1° intervals of ionospheric colatitude between 6° and 11° in the northern hemisphere and 6° and 13° in the southern. Data in overlapping 2° colatitude intervals are used in section 4.4 to investigate the polar oscillations, with results shown in Figure 12.

magnetosphere than those shown in Figure 1. In the poleward region, ~5°–11° colatitude, the southern data show currents of consistently opposite sign to those at large colatitude, corresponding to the southern PPO polar oscillations in the south, while the northern data show only small variable values, again consistent with the absence of southern PPO oscillations in the northern polar region.

4.4. Latitude Variation of the Equatorial Oscillations

The theoretical model of the PPO current system proposed by *Southwood and Kivelson* [2007] envisaged strict hemisphere-to-hemisphere field-aligned currents that would produce a perturbation field essentially symmetric about the magnetic equator. The current systems in Figures 1c–1h, following *Andrews et al.* [2010a, 2010b] and *Southwood and Cowley* [2014], generalize that picture by admitting the closure of current across the field in the body of the magnetosphere, thereby transmitting a force to the plasma, which would result in the PPO field perturbations reducing in amplitude along field lines from the generating hemisphere. Our results in Figures 5b and 5f show northern system oscillations in the north and southern system oscillations in the south that are of comparable amplitude, while Figures 5h and 5d show northern oscillations in the south that are weaker by a factor of ~2.5, and southern oscillations in the north that that are weaker by a factor of ~1.2. In this section we examine in detail the variation of the oscillation amplitudes with latitude along the equatorial field lines.

We focus on a flux shell located just equatorward of the region of PPO-related field-aligned currents for which we have good latitude coverage, specifically those mapping to the northern ionosphere between 20° and 26° colatitude (dotted lines in Figure 3a), and correspondingly to the southern ionosphere between 22.1° and 28.8° (dotted lines in Figure 3c), as employed previously in Figure 5. This flux shell is shown shaded gray in the meridian plane view in Figure 10 and extends between 3.8 and 6.6 R_S in the equatorial plane. The colored lines show periapsis segments of the Cassini trajectory mapped into the meridian in cylindrical (ρ, z) coordinates, color-coded as in previous figures, while the radial lines indicate lines of constant latitude ± 45° about the equator. As indicated above, it can be seen that there is good coverage of the flux shell over this latitude range. We then divide the field data within the shell into overlapping latitude intervals that are 15° wide and step by 7.5° as shown, with centers located between ±37.5°. We map the data in the flux shell from each latitude interval along the field lines into the northern ionosphere using equation (3), this to take account of the variation associated with the convergence of the field-aligned currents toward the planetary poles. With regard to the related results shown in Figure 5, fitted to one oscillation at a time, we note that mapping a field

value into the northern ionosphere rather than the southern, as for the southern data in Figures 5e–5h, increases its value by ~10%, due to the stronger planetary field in the north than in the south. Here we fit these mapped data to the two-oscillation function

$$B'_{\varphi i}(\varphi, t) = \langle B_{\varphi i} \rangle + B_{\varphi i0N} \sin(\Phi_N(t) - \varphi - \Delta\Phi_N) + B_{\varphi i0S} \sin(\Phi_S(t) - \varphi - \Delta\Phi_S), \quad (9)$$

where $\langle B_{\varphi i} \rangle$ is a constant term, $B_{\varphi i0N,S}$ are the northern and southern system oscillation amplitudes, $\Phi_{N,S}(t)$ are the corresponding phases, specifically those of *Andrews et al*. [2012], φ is the azimuth of the spacecraft measured from noon in the sense of planetary rotation, and $\Delta\Phi_{N,S}$ are possible phase offsets from the *Andrews et al*. [2012] model, as in Figure 5 and previously in *Hunt et al*. [2014]. The results in Figures 5b and 5f suggest, for example, that appropriate offsets may be $\Delta\Phi_N \approx -30°$ and $\Delta\Phi_S \approx +15°$.

The basis of the fitting method is as follows. For a given latitude data set we first fix the pair of phase offsets $\Delta\Phi_{N,S}$ at likely values, and then search for the values of the three parameters within a data cube, $\langle B_{\varphi i} \rangle$ in steps of 2.5 nT, and $B_{\varphi i0N,S}$ in steps of 1 nT, that give the minimum RMS deviation between the data and the model in equation (9). We then vary the values of $\Delta\Phi_{N,S}$ in steps of 5° to find the values that give the smallest overall RMS deviation over the whole data set. These values were found to be $\Delta\Phi_N = -30°$ and $\Delta\Phi_S = +10°$, which were used throughout in the determination of the other three parameters, yielding the results shown in Figure 11. Figure 11a shows the latitude profile of the RMS deviation between the data and the model, Figure 11b the mean value $\langle B_{\varphi i} \rangle$ in equation (9), Figure 11c the amplitude of the northern system oscillation $B_{\varphi i0N}$ (blue) and southern system oscillation $B_{\varphi i0S}$ (red), and Figure 11d the amplitude ratio $k = B_{\varphi i0N}/B_{\varphi i0S}$, where the vertical scale is linear in k from 0 to 1 in the lower half of the figure and linear in $1/k = k'$ between 1 and 0 in the upper half, thereby covering all possible values of k from zero to infinity. As in Figure 5, the uncertainty in each parameter was determined by implementation of the jackknife statistical resampling method, described in section 4.1, in which one contributing Rev is removed at a time, with the uncertainty being determined from the modified standard deviation of the set of fitted parameters. These uncertainties have also been verified for several latitude intervals by the more intensive bootstrap resampling method. We note that the RMS deviation values in Figure 11a are generally smaller than those in Figure 5 when fitting to a single oscillation function, thus indicating that the combination of two oscillations in equation (9) provides a better overall fit to the data.

Figure 11c shows that the mapped northern system amplitude peaks at ~33 nT at the highest northern latitude examined, centered at +37.5°, and then decreases monotonically with decreasing latitude to ~6 nT at -37.5°, consistent with zero within uncertainties. This behavior is consistent with the values determined from the single-oscillation analyses in Figures 5b and 5h. Likewise, the southern system amplitude peaks at the larger value of ~43 nT at the highest southern latitude examined, centered at -37.5°, decreases monotonically with increasing latitude to ~22 nT near the equator, and then remains nearly constant within the uncertainties at ~20 nT in the northern hemisphere. This behavior is also consistent with the values determined from the single-oscillation analyses in Figures 5f and 5d. Overall, the southern oscillations are seen to dominate the northern at high southern latitudes, fall to comparable values to the northern just north of the equator, and then remain modestly smaller than the northern oscillations throughout the northern hemisphere. This is shown explicitly in Figure 11d, where the amplitude ratio k falls near-linearly (using the scales shown) from $k' = 0.5$ at the northernmost latitudes examined (i.e., $k = 2$), to near zero in the southernmost. These results show that the PPO-related field-aligned currents close cross-field in the magnetospheric plasma, nearly wholly for the northern system in the interval studied here, and at least partially for the southern system, mainly in the southern hemisphere in that case.

Figure 11b also shows that the mean azimuthal field $\langle B_{\varphi i} \rangle$ has small and positive values in the northern hemisphere, consistent with the results in Figures 5b and 5d, falling to small negative values south of the equator, consistent with results in Figures 5f and 5h (and with *Hunt et al*. [2014]). These perturbations form an otherwise unexpected weak leading field configuration, located well equatorward of the main "lagging" field region that terminates near ~19° northern colatitude (Figure 7a), mapping to ~7.6 R_s in the equatorial plane. Previously, *Hunt et al*. [2014] suggested that this field could be due to a phase asymmetry in the PPO field perturbations, which makes the negative half cycle of the southern system B_φ oscillation slightly larger in amplitude than the positive half cycle, associated with a latitudinal motion of the southern system currents to higher latitudes and outward displacement in the equatorial plane in the downward current sector at $\Psi_S = 90°$ (positive equatorial B_φ), and to lower latitudes and inward displacement in the equatorial plane in the upward current sector at $\Psi_S = 270°$ (negative equatorial B_φ). The same effect would produce the opposite asymmetry for the northern

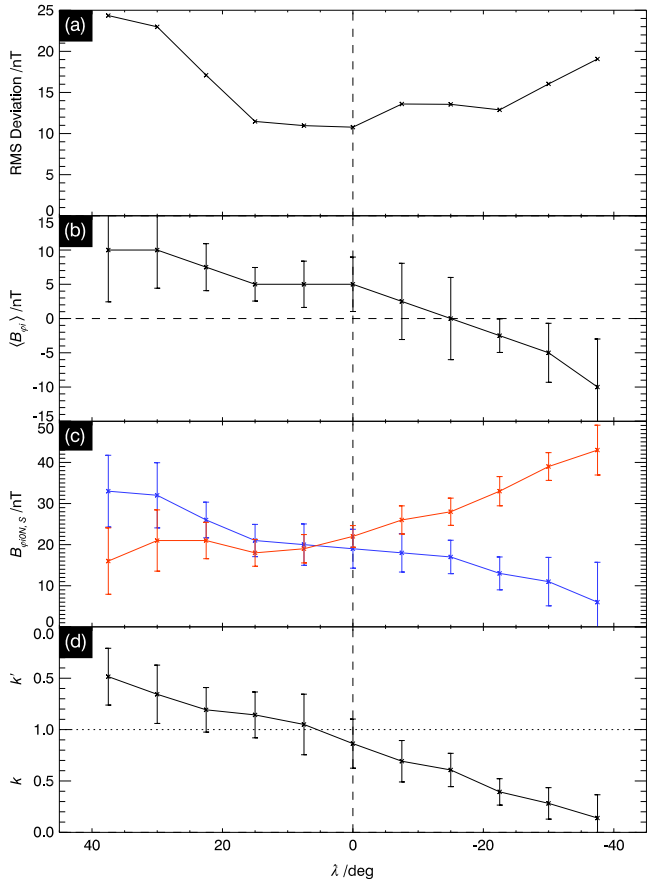

Figure 11. (a–d) Plots showing the latitude variation of oscillation parameters in the flux shell shown gray in Figure 10. These were determined from fits of equation (9) to the northern-mapped azimuthal field data in overlapping 15° intervals of latitude centered between ±37.5° (see Figure 10), using $\Delta\Phi_N = -30°$ and $\Delta\Phi_S = +10°$. Figure 11a shows the minimum RMS deviation (nT) corresponding to the best fit parameters shown, Figure 11b the mean value Ψ_S (nT), Figure 11c the amplitudes of the northern (blue) and southern (red) PPO oscillations $B_{\varphi i0N,S}$, and Figure 11d the north/south amplitude ratio $k = B_{\varphi i0N}/B_{\varphi i0S}$, the vertical scale being linear in k from 0 to 1 in the lower half and linear in $1/k = k'$ between 1 and 0 in the upper half. The uncertainties in the fitted parameters have been determined using the jackknife statistical resampling method described in section 4.1. The vertical dashed line indicates the equator.

system, associated with a latitudinal motion of the northern system currents to lower latitudes and inward displacement in the equatorial plane in the upward current sector at $\Psi_N = 90°$ (positive equatorial B_φ), and to higher latitudes and outward displacement in the equatorial plane in the downward current sector at $\Psi_N = 270°$ (negative equatorial B_φ). A dominant northern system in the northern hemisphere and southern system in the southern hemisphere would then produce a reversal in sense of the mean azimuthal field across the equator as found, although we note that the reversal in the amplitude ratio occurs north of the equator while the reversal in the mean azimuthal field occurs to its south.

We now undertake a similar two-oscillation analysis of the mapped polar azimuthal field data, noting that no oscillations from "opposite" hemispheres were detected in the analyses shown in Figure 5, nor in previous related studies within an ~10% observational limit by amplitude [e.g., *Andrews et al.*, 2012]. In this case we employ data observed within overlapping 2° bins of ionospheric colatitude, centered between 7° and 10° in the northern hemisphere and 7° and 12° in the southern (see also Figure 3), whose corresponding polar flux shells and traversing Cassini Revs are also shown in Figure 10. Results are shown in Figures 12a–12d and 12e–12h for the northern and southern polar regions, respectively, in a similar format to Figure 11, showing from top to bottom the RMS deviation of the fits to equation (9), the mean values $\langle B_{\varphi i}\rangle$, the northern (blue) and southern (red) amplitudes $B_{\varphi i0N,S}$, and the modulus of the amplitude ratios (north/south). For the northern data we determined a best fit northern phase offset of $\Delta\Phi_N = 0°$ consistent with Figure 5b, while for the southern data the best fit offset was found to be $\Delta\Phi_S = 55°$, consistent with Figure 5e (~51°) and *Hunt et al.* [2014] (~47°). In both cases, however, we have no a priori knowledge of the corresponding phase offset for oscillations from the opposite hemisphere, so we have simply set these phase offsets to zero, but allow the fitted amplitude to have either a positive or negative sign (the latter equivalent to taking a phase offset of 180°), on the basis that we do not know whether such oscillations might be essentially in phase or in antiphase with those at lower latitudes. The key results are shown in Figures 12c and 12g, where we see that the amplitudes from the opposite hemisphere are essentially consistent with zero throughout, even switching sign from positive to negative with increasing colatitude in the southern hemisphere. The modulus amplitude ratios are $k' = (1/k) \approx 0 - 0.2$ in the northern hemisphere in Figure 12d and $k \approx 0$–0.3 in the southern hemisphere in Figure 12h, generally consistent with zero. The other parameters in Figure 12 are in line with expectation based Figures 3 and 5, where in particular

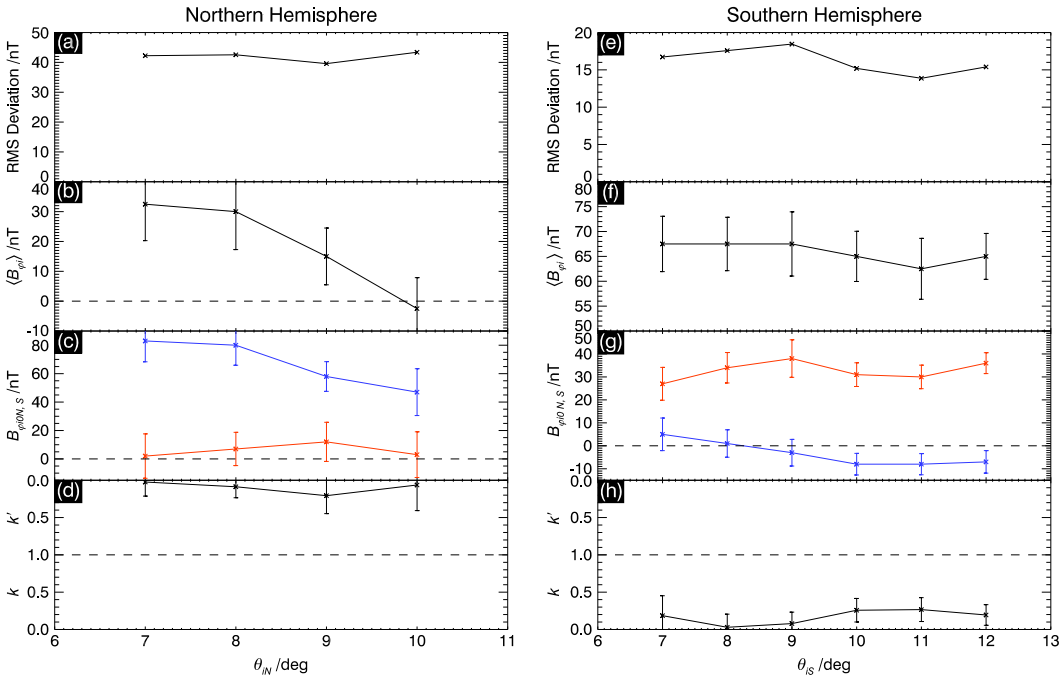

Figure 12. Plots in the same format as Figure 11 showing the best two-oscillation fits to equation (9) for mapped polar azimuthal field data in overlapping 2° intervals of northern (left) and southern (right) ionospheric colatitudes, the field data being mapped to the corresponding ionosphere. The phase offsets employed were $\Delta\Phi_N = 0°$ and $\Delta\Phi_S = 0°$ in the northern hemisphere, and $\Delta\Phi_N = 0°$ and $\Delta\Phi_S = 55°$ in the southern, though we also allow the amplitude of the oscillation from the opposite hemisphere to take negative values thus allowing for a possible 180° phase change in the polar region. As in Figure 11, the uncertainties have been estimated by an implementation of the jackknife method.

we note that the RMS deviations in the northern data in Figure 12a are essentially the same as in the single-oscillation analysis in Figure 5a, while that in the northern data in Figure 12e is essentially the same as that in Figure 5e. Inclusion of a second period thus makes little difference to the degree of model fit to the data in these cases, unlike the equatorial case shown in Figure 11.

4.5. PPO-Independent Current System and Plasma Subcorotation

We now consider the northern PPO-independent current profile and its relation to the subcorotation of magnetospheric plasma, discussed in section 1, following the analysis for the southern hemisphere presented by *Hunt et al.* [2014] in their section 6.1. The ionospheric meridional Pedersen current associated with near-axisymmetric subcorotation of the magnetospheric plasma is given by [see *Cowley et al.*, 2008, and references within]

$$I_m = \frac{\Sigma_P^* \rho_i^2 B_i \Omega_S}{\cos \alpha_i} \left(1 - \frac{\omega}{\Omega_S}\right), \tag{10}$$

where Ω_S is the angular velocity of the planet, ω is the angular velocity of the plasma (constant along a field line for an approximately axisymmetric field), B_i is the ionospheric magnetic field strength, α_i is the angle between the ionospheric field and the local vertical, ρ_i is the perpendicular distance of the ionosphere from the planet's rotation axis, and Σ_P^* is the effective height-integrated ionospheric Pedersen conductivity. The latter parameter is reduced from the true value Σ_P if neutral winds are generated in the Pedersen layer due to the drag of ion-neutral collisions. These conductivities are related by

$$\Sigma_P^* = (1 - k)\Sigma_P, \tag{11}$$

where

$$k = \left(\frac{1 - \left(\Omega_S^*/\Omega_S\right)}{1 - \left(\omega/\Omega_S\right)}\right), \tag{12}$$

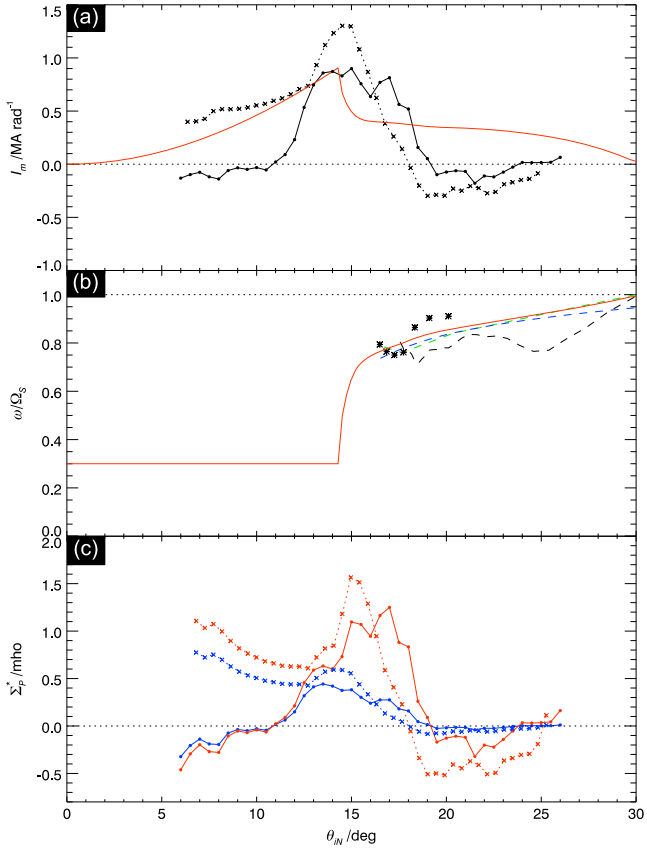

Figure 13. (a–c) Plots showing northern colatitude profiles of the PPO-independent ionospheric meridional current, plasma angular velocity, and effective Pedersen conductivity. In Figure 13a the black circles joined by solid lines and the crosses joined by dotted lines show the northern and mapped southern PPO-independent meridional current profiles (MA rad^{-1}), respectively, as in Figure 9a. The red line shows a theoretical meridional current profile derived using equation (10) and the empirical plasma angular velocity profile shown in Figure 13b (red line), assuming a fixed effective Pedersen conductivity of 0.6 mho. For details of the sources employed to construct the empirical angular velocity profile see the text in section 4.5. The plasma angular velocity is shown normalized to Saturn's angular velocity Ω_S, taken to correspond to the IAU System III rotation period, such that the horizontal dotted line at unity represents rigid corotation of the plasma. In Figure 13c the red circles joined by solid lines show a colatitude profile of the effective Pedersen conductivity of the northern ionosphere (mho), calculated from the northern meridional current profile in Figure 13a using equation (13) together with the angular velocity profile in Figure 13b, while the blue circles and solid lines show minimum conductivity values obtained by putting $\omega/\Omega_S = 0$ into this equation. The red and blue crosses and dotted lines show the corresponding southern conductivity profiles similarly calculated using the mapped southern meridional current profile in Figure 13a.

And Ω_S^* the angular velocity of the neutral atmosphere in the Pedersen layer. Modeling has shown that an appropriate value for Saturn is $k \approx 0.5$ [*Galand et al*., 2011].

Figure 13a shows the northern PPO-independent current profile in Figure 7a and 9a (black dots and solid lines) together with the profile expected for a fixed value of Σ_P^* (red) combined with the empirical plasma angular velocity profile in Figure 13b. We also show (black crosses and dotted lines) the corresponding profile mapped from the southern hemisphere from Figure 9a. The value of Σ_P^* has been somewhat arbitrarily set at 0.6 mho, such that the theoretical profile agrees with observed values in the poleward part of the main current region. The normalized empirical angular velocity profile in Figure 13b (red) is the same as that in *Hunt et al*. [2014], but now mapped along field lines into the northern hemisphere. It is based on magnetospheric ion velocities determined by *Wilson et al*. [2009] and *Thomsen et al*. [2014] (black dashed lines and stars, respectively), ion and electron plasma injection dispersion signatures analyzed by *Müller et al*. [2010] (green dashed line), the rotation of plasma "blobs" determined by *Carbary and Mitchell* [2014], further ion measurements in the outer nightside magnetosphere discussed by *Thomsen et al*. [2014], and the theoretical model of *Cowley et al*. [2004b] at polar latitudes where we take the constant value $\omega/\Omega_S = 0.3$ (see *Hunt et al*. [2014] for further discussion). The dotted line at $\omega/\Omega_S = 1$ represents rigid plasma corotation, where Ω_S is taken to correspond to the IAU System III rotation period of 10.65622 h based on a slightly modified version of the principal period determined from Voyager SKR data by *Desch and Kaiser* [1981].

Given this angular velocity profile, the consequent red current profile in Figure 13a derived from equation (10) with fixed conductivity indicates distributed downward currents over the polar region, a layer of strong upward current at the OCB where the angular velocity of the plasma suddenly increases, followed by a more distributed region of weaker upward current at larger colatitudes, similar to the theoretical models of *Cowley and Bunce* [2003] and *Cowley et al*. [2004a, 2004b] derived on an essentially equivalent basis. Comparison with the observed northern current profile in Figure 13a suggests, however, that variations of the effective Pedersen conductivity in the northern ionosphere must also play an important role, with conductivities much

smaller than 0.6 mho at polar latitudes (~5°–11°), and equatorward of the main current region (beyond ~19°), where no counterpart of the theoretical weaker secondary region of upward current is present in the data. Larger conductivities are implied, however, in the equatorward part of the main current region (~15°–18°). Comparison with the southern profile indicates similar features in the equatorward region, but much better agreement with the form of the theoretical profile at polar latitudes.

We examine this in more detail by inverting equation (10) to derive Σ_P^* from the observed current profiles and the empirical angular velocity model, given by

$$\Sigma_P^* = \frac{\cos\alpha_i I_m}{\rho_i^2 B_i \Omega_S \left(1 - \frac{\omega}{\Omega_S}\right)}. \tag{13}$$

Results derived from the northern current data using the empirical angular velocity profile are shown in Figure 13c by the red dots and solid line, while the blue dots and solid line shows the minimum possible Σ_P^* value obtained by putting $\omega/\Omega_S = 0$ in equation (13) (assuming negative values do not occur). The equivalent profiles obtained from the southern data are shown by the red and blue crosses joined by dotted lines, mapped along field lines into the northern hemisphere for comparison. It can be seen that the inferred conductivities in the main current region at ~14° to ~18° colatitude peak at similar values ~1.2 mho in the north and ~1.6 mho in the south, which, as in *Hunt et al*. [2014], we presume is due to precipitation of auroral electrons in the region generally containing upward field-aligned currents. We note that this region generally corresponds to the outer region of hot magnetospheric electrons in ELS data (Figure 4). In the equatorward region, however, where the inferred ionospheric current falls to small (and negative) values despite the well-documented occurrence of significant plasma subcorotation, the implication is that the effective conductivity of the ionosphere becomes at least an order of magnitude smaller, though of course the negative values derived from the current profile here are not physically meaningful.

Similarly on open field lines poleward of ~13°–14° colatitude, the currents and hence the inferred conductivity also fall to small (and negative) values poleward of ~11°, again suggestive of conductivities at least an order of magnitude smaller than in the main current region, unlike those inferred in the southern hemisphere. Since the ELS electron data (see Figure 4) indicate the lack of hot electrons in these regions in the majority of the data set, this is likely connected with the pre vernal equinox conditions prevailing in the interval, during which Saturn's northern spin axis was tilted by between ~8° and ~4° away from the Sun. The northern ionosphere at smaller colatitudes was thus in permanent darkness, but subject to increasing episodes of daily insolation at larger colatitudes. As in *Hunt et al*. [2014], these results show that the latitudinal variations in the effective Pedersen conductivity of the ionosphere are equally or even more important in defining the structure of the PPO-independent field-aligned current system as the changes in angular velocity of the equatorial magnetospheric plasma.

5. Summary and Conclusions

In this paper we have provided a first detailed analysis of the PPO-dependence of field-aligned currents in Saturn's northern hemisphere, employing azimuthal component magnetic field data from a set of pre equinox Cassini periapsis passes during 2008 over the post dusk to pre midnight sector of the northern auroral region. As in the related study by *Hunt et al*. [2014] of the passes on these orbits over the midnight to post midnight sectors of the southern auroral region, we separate the current into components that do and do not depend on the PPO phase by using the symmetries involved, where the PPO currents are taken to vary approximately sinusoidally with the PPO phase. The PPO-independent current is then taken to relate to plasma subcorotation in the magnetosphere. Our principal results are summarized as follows.

1. During the 2008 epoch the field-aligned currents in the northern hemisphere are not only strongly modulated in form and magnitude by the northern PPO system in a similar manner to those in the southern hemisphere are modulated by the southern PPO system as found by *Hunt et al*. [2014], but in the closed field region (not the polar) they are also significantly modulated by the southern PPO system as well. This provides the first direct observational evidence for the PPO-related inter-hemispheric currents proposed

theoretically by *Southwood and Kivelson* [2007] and later refined by *Southwood and Cowley* [2014]. As a consequence, while the current structures in the north are clearly similar to those in the south, they have much less regularity in form than the usually well-ordered four-sheet structures observed in the south. Using these data we were unable to discern the regular PPO-related ~2° colatitude modulation in the position of the current layers that is a feature of the southern data.

2. The meridional current profile of the northern PPO-independent system (positive equatorward) determined from the field data is found to have small (and negative) values at highest polar latitudes, but increases sharply between ~11° and ~13.5° northern colatitude on open field lines (the mean OCB in the north lies at ~13.3° according to *Jinks et al*. [2014]), implying a downward current flow of ~1 MA rad^{-1} in this region, with a corresponding current density of ~25 nA m^{-2}. Assuming axisymmetry, the peak total equatorward current flow in this system is thus ~6 MA. The meridional current then falls toward small (and negative) values between ~17° and ~19°, implying an essentially equal and opposite upward current flow of ~1 MA rad^{-1} in this region, with a corresponding ionospheric current density also of ~25 nA m^{-2}. The latter current maps between ~7.5 and ~11 R_s in the equatorial magnetosphere, spanning the inner part of the main hot plasma region. This is similar to the PPO-independent current system in the south, though the peak meridional current values are somewhat larger in the south, and falloff much more slowly with decreasing colatitude in the polar region, extending over the whole polar region observed in that case. This difference likely results from the preequinox conditions prevailing at the time of these measurements, with the northern polar axis tilted between ~4° and ~8° away from the Sun.
3. Combining the PPO-independent meridional current profile with an empirical plasma angular velocity profile suggests that the effective height-integrated ionospheric Pedersen conductivity of the ionosphere is ~0.1 mho or less in the poleward-most region of low current flow, increasing to ~0.6 mho in the outer open field region where significant currents are first observed (~11°–13.5° colatitude). The conductivity then increases further on closed field lines, peaking at ~1.2 mho at ~17° colatitude, before falling sharply back to small values ~0.1 mho or less at ~19° equatorward of the main current region. These results again indicate that, as in the south, the variations of the PPO-independent meridional current, and hence of the field-aligned currents, are as strongly influenced by variations in the ionospheric conductivity as by the variations in plasma angular velocity.
4. The northern PPO-related field-aligned current consists of a main layer of either upward (for PPO phase $\Psi_N \approx 90°$) or downward (for $\Psi_N \approx 270°$) current, of peak magnitude ~1.5 MA rad^{-1}, flowing between ~12° and ~18° northern colatitude, essentially co-located with the region of PPO-independent current, which separate the oppositely-directed PPO-related azimuthal fields in the polar region from those on closed field lines at larger colatitudes. The total current flowing in the system, equal and opposite in the two "halves' of the cycle, is thus ~3.5 MA, directly comparable to the current flowing in the PPO-independent system in the same region. The associated ionospheric current density is ~20 nA m^{-2}. A second current layer of opposite polarity is located immediately equatorward of the main layer, between ~18° and ~21.5°, which carries ~1 MA rad^{-1} (with a total half-cycle current of ~2 MA), which strongly reduces the magnitude of the PPO-related currents and fields at larger colatitudes. This current has an ionospheric density of ~15 nA m^{-2}, and maps between ~6 and ~9 R_s in the equatorial plane.
5. The main southern PPO-related field-aligned current is essentially co-located with the northern PPO-related current between ~11.5° and ~18.5° northern colatitude, and hence with the PPO-independent current, directed upward (for PPO phase $\Psi_S \approx 90°$) or downward (for $\Psi_S \approx 270°$), with peak magnitude ~1.25 MA rad^{-1}. The total current flowing in a half-cycle is thus ~3 MA, with a corresponding current density of ~15 nA m^{-2}. A current of opposite polarity and magnitude ~0.35 MA rad^{-1} flows at the poleward border of this system at ~11.5°, with a half-cycle current of ~0.75 MA, that switches off the southern system perturbations in the north polar region. A larger current of opposite polarity and peak magnitude ~0.75 MA rad^{-1} also flows in the region immediately equatorward between ~18.5° and ~22°, again reducing the magnitude of the perturbations at lower latitudes. The half-cycle total current is thus ~1.5 MA, with an associated ionospheric current density of ~10 nA m^{-2}. Comparison of the southern system field-aligned currents flowing in the northern and southern ionosphere shows that the main PPO currents are of comparable magnitude, ~1.25 MA rad^{-1} as above, though spread further poleward in the north than the south, but that the equatorward secondary currents are smaller in the south than the north by

a factor of almost two, such that the southern oscillations in the interior region at lower latitudes are stronger in the south than in the north. This finding indicates that the PPO currents involve somewhat more complexity than present theoretical pictures would suggest.

6. Investigation of the latitude dependence of the oscillations observed interior to the main field-aligned current layers, on flux tubes mapping into the northern ionosphere between 20° and 26°, and correspondingly into the southern hemisphere between 22.1° and 28.8° (3.8 to 6.6 R_s in the equatorial plane), shows that the northern oscillations fall in amplitude gradually but continuously from the highest northern latitudes observed (~40°) to near-zero at corresponding latitudes in the south. The southern oscillations are thus dominant at such high southern latitudes, but also fall with increasing latitude to become comparable with the northern oscillations in the equatorial region, and modestly lower than the northern oscillations at higher northern latitudes (consistent with point 5 above). These variations show that the associated field-aligned currents gradually reduce in magnitude with distance along field lines from the corresponding hemisphere, feeding cross-field currents that flow in the magnetosphere.
7. A related investigation of the polar oscillations confirms the absence of field perturbations associated with the opposite hemisphere found in previous studies [e.g., *Andrews et al*., 2012], to within a ~10% observational limit by amplitude. It was also found that the northern polar oscillations lag in phase by ~30° compared with the northern oscillations equatorward of the field-aligned current layers, similar to the ~50° polar lag for the southern oscillations found previously by *Hunt et al*. [2014]. The PPO phases generated by *Andrews et al*. [2012] correspond most closely to those of the equatorial oscillations for the southern system, but to the polar oscillations of the northern system.

These results thus show that for the preequinox interval investigated, while the field-aligned currents in the southern hemisphere are dominantly modulated by the southern PPO system, both northern and southern systems modulate the northern currents, with the effect of the southern currents being only modestly smaller than those of the northern. They also show the presence of secondary PPO-related currents of opposite polarity flowing in the region equatorward of the main PPO current, a feature more weakly indicated in the southern data. The implications for auroral modulation in the north compared with the south remain to be investigated. Future work is also needed to extend these results and those of *Hunt et al*. [2014] to other local times and other Saturn seasons. The results will be important for the assessment of the unique observations that will be made during Cassini's Grand Finale mission in 2016–17.

Appendix A: Hemispheric Ratio of Subcorotation Pedersen Currents on a Given Field Line

We consider the relationship of the meridional ionospheric currents in the northern and southern hemispheres associated with subcorotation of the magnetospheric plasma on closed field lines, where in the steady state the plasma angular velocity at conjugate points must be the same. Following the methodology of *Cowley and Bunce* [2003] which takes account of the north-south differences in the planetary ionospheric magnetic field and the polar flattening of the planetary atmosphere and ionosphere, we rearrange equation (10) into the form

$$I_m(\theta_i) = \Sigma_P^* \Omega_S \left(1 - \frac{\omega}{\Omega_S}\right) \left(\frac{B_i(\theta_i)\rho_i^2(\theta_i)}{\cos\alpha_i(\theta_i)}\right), \tag{A1}$$

Where θ_i is the colatitude in the ionosphere. Given that the plasma angular velocity must be the same at the two ends of a closed field line, the ratio of the horizontal meridional Pedersen currents at conjugate points thus depends on the relative values of the effective Pedersen conductivity Σ_P^*, and the quantity in the final bracket in equation (A1) that depends only on the conjugate properties of the planetary magnetic field within the ionosphere. We have therefore evaluated the latter quantity at conjugate points using the *Burton et al*. [2010] planetary field model, and have determined the south/north ratio versus ionospheric colatitude. This ratio has a value of unity at the poles, 0.9978 at 10° northern colatitude (southern value slightly smaller than northern), decreasing to 0.9905 at 20°, and to 0.9763 at 30°. The departure from unity in the region of interest is therefore small, such that the ratio of meridional Pedersen currents will depend principally on the relative values of Σ_P^* in the northern and southern ionospheres.

Acknowledgments
Work at Leicester was supported by STFC Consolidated grant ST/K001000/1, work at UCL-MSSL by STFC Consolidated grant ST/K000977/1, and work at SINP MSU by RFBR grant 12-05-00219-a. G.J.H. was supported by STFC Quota Studentship ST/K502121/1. E.J.B. was supported by the award of the Philip Leverhulme Prize. CAPS-ELS operations were supported by ESA via the UK Space Agency. We thank S Kellock and the Cassini Mag team at Imperial College for access to processed magnetometer data, J.F. Carbary for access to the UV auroral boundary data shown in Figures 2c and 2d, and M.F. Thomsen for access to ion velocity measurements employed in Figure 14b. Calibrated data from the Cassini mission are available from the NASA Planetary Data System at the Jet Propulsion Laboratory (https://pds.jpl.nasa.gov/).

Michael Liemohn thanks the reviewers for their assistance in evaluating the paper.

References

Andrews, D. J., E. J. Bunce, S. W. H. Cowley, M. K. Dougherty, G. Provan, and D. J. Southwood (2008), Planetary period oscillations in Saturn's magnetosphere: Phase relation of equatorial magnetic field oscillations and SKR modulation, *J. Geophys. Res.*, *113*, A09205, doi:10.1029/2007JA012937.

Andrews, D. J., S. W. H. Cowley, M. K. Dougherty, and G. Provan (2010a), Magnetic field oscillations near the planetary period in Saturn's equatorial magnetosphere: Variation of amplitude and phase with radial distance and local time, *J. Geophys. Res.*, *115*, A04212, doi:10.1029/2007JA014729.

Andrews, D. J., A. J. Coates, S. W. H. Cowley, M. K. Dougherty, L. Lamy, G. Provan, and P. Zarka (2010b), Magnetospheric period oscillations at Saturn: Comparison of equatorial and high-latitude magnetic field periods with north and south SKR periods, *J. Geophys. Res.*, *115*, A12252, doi:10.1029/2010JA015666.

Andrews, D. J., B. Cecconi, S. W. H. Cowley, M. K. Dougherty, L. Lamy, G. Provan, and P. Zarka (2011), Planetary period oscillations in Saturn's magnetosphere: Evidence in magnetic field phase data for rotational modulation of Saturn kilometric radiation emissions, *J. Geophys. Res.*, *116*, A09206, doi:10.1029/2011JA016636.

Andrews, D. J., S. W. H. Cowley, M. K. Dougherty, L. Lamy, G. Provan, and D. J. Southwood (2012), Planetary period oscillations in Saturn's magnetosphere: Evolution of magnetic oscillation properties from southern summer to post-equinox, *J. Geophys. Res.*, *117*, A04224, doi:10.1029/2011JA017444.

Belenkaya, E. S., S. W. H. Cowley, S. V. Badman, M. S. Blokhina, and V. V. Kalegaev (2008), Dependence of the open-closed field line boundary in Saturn's ionosphere on both the IMF and solar wind dynamic pressure: Comparison with the UV auroral oval observed by the HST, *Ann. Geophys.*, *26*, 159–166, doi:10.5194/angeo-26-159-2008.

Bunce, E. J., S. W. H. Cowley, I. I. Alexeev, C. S. Arridge, M. K. Dougherty, J. D. Nichols, and C. T. Russell (2007), Cassini observations of the variation of Saturn's ring current parameters with system size, *J. Geophys. Res.*, *112*, A10202, doi:10.1029/2007JA012275.

Bunce, E. J., et al. (2010), Extraordinary field-aligned current signatures in Saturn's high-latitude magnetosphere: Analysis of Cassini data during Revolution 89, *J. Geophys. Res.*, *115*, A10238, doi:10.1029/2010JA015612.

Burton, M. E., M. K. Dougherty, and C. T. Russell (2010), Saturn's internal planetary magnetic field, *Geophys. Res. Lett.*, *37*, L24105, doi:10.1029/2010GL045148.

Carbary, J. F. (2012), The morphology of Saturn's ultraviolet aurora, *J. Geophys. Res.*, *117*, A06210, doi:10.1029/2012JA017670.

Carbary, J. F., and D. G. Mitchell (2013), Periodicities in Saturn's magnetosphere, *Rev. Geophys.*, *51*, 1–30, doi:10.1002/rog.20006.

Carbary, J. F., and D. G. Mitchell (2014), Keogram analysis of ENA images at Saturn, *J. Geophys. Res. Space Physics*, *119*, 1771–1780, doi:10.1002/2014JA019784.

Cowley, S. W. H., and E. J. Bunce (2003), Corotation-driven magnetosphere-ionosphere coupling currents in Saturn's magnetosphere and their relation to the auroras, *Ann. Geophys.*, *21*, 1691–1707.

Cowley, S. W. H., E. J. Bunce, and R. Prangé (2004a), Saturn's polar ionospheric flows and their relation to the main auroral oval, *Ann. Geophys.*, *22*, 1379–1394.

Cowley, S. W. H., E. J. Bunce, and J. M. O'Rourke (2004b), A simple quantitative model of plasma flows and currents in Saturn's polar ionosphere, *J. Geophys. Res.*, *109*, A05212, doi:10.1029/2003JA010375.

Cowley, S. W. H., D. M. Wright, E. J. Bunce, A. C. Carter, M. K. Dougherty, G. Giampieri, J. D. Nichols, and T. R. Robinson (2006), Cassini observations of planetary-period magnetic field oscillations in Saturn's magnetosphere: Doppler shifts and phase motion, *Geophys. Res. Lett.*, *33*, L07104, doi:10.1029/2005GL025522.

Cowley, S. W. H., C. S. Arridge, E. J. Bunce, J. T. Clarke, A. J. Coates, M. K. Dougherty, J.-C. Gérard, D. Grodent, J. D. Nichols, and D. L. Talboys (2008), Auroral current systems in Saturn's magnetosphere: Comparison of theoretical models with Cassini and HST observations, *Ann. Geophys.*, *26*, 2613–2630.

Desch, M. D., and M. L. Kaiser (1981), Voyager measurement of the rotation period of Saturn's magnetic field, *Geophys. Res. Lett.*, *8*, 253–256, doi:10.1029/GL008i003p00253.

Espinosa, S. A., and M. K. Dougherty (2000), Periodic perturbations in Saturn's magnetic field, *Geophys. Res. Lett.*, *27*, 2785–2788, doi:10.1029/2000GL000048.

Espinosa, S. A., D. J. Southwood, and M. K. Dougherty (2003), Reanalysis of Saturn's magnetospheric field data view of spin-periodic perturbations, *J. Geophys. Res.*, *108*(A2), 1085, doi:10.1029/2001JA005083.

Galand, M., L. Moore, I. Mueller-Wodarg, M. Mendillo, and S. Miller (2011), Response of Saturn's auroral ionosphere to electron precipitation: Electron density, electron temperature, and electrical conductivity, *J. Geophys. Res.*, *116*, A09306, doi:10.1029/2010JA016412.

Galopeau, P. H. M., and A. Lecacheux (2000), Variations of Saturn's radio rotation period measured at kilometer wavelengths, *J. Geophys. Res.*, *105*, 13,089–13,101, doi:10.1029/1999JA005089.

Gurnett, D. A., A. Lecacheux, W. S. Kurth, A. M. Persoon, J. B. Groene, L. Lamy, P. Zarka, and J. F. Carbary (2009a), Discovery of a north–south asymmetry in Saturn's radio rotation period, *Geophys. Res. Lett.*, *36*, L16102, doi:10.1029/2009GL039621.

Gurnett, D. A., A. M. Persoon, J. B. Groene, A. J. Kopf, G. B. Hospodarsky, and W. S. Kurth (2009b), A north–south difference in the rotation rate of auroral hiss at Saturn: Comparison to Saturn's kilometric radio emission, *Geophys. Res. Lett.*, *36*, L21108, doi:10.1029/2009GL040774.

Gurnett, D. A., A. M. Persoon, J. B. Groene, W. S. Kurth, M. Morooka, J.-E. Wahlund, and J. D. Nichols (2011), The rotation of the plasmapause-like boundary at high latitudes in Saturn's magnetosphere and its relation to the eccentric rotation of the northern and southern auroral ovals, *Geophys. Res. Lett.*, *38*, L21203, doi:10.1029/2011GL049547.

Hunt, G. J., S. W. H. Cowley, G. Provan, E. J. Bunce, I. I. Alexeev, E. S. Belenkaya, V. V. Kalegaev, M. K. Dougherty, and A. J. Coates (2014), Field-aligned currents in Saturn's southern nightside magnetosphere: Subcorotation and planetary period oscillation components, *J. Geophys. Res. Space Physics*, *119*, 9847–9899, doi:10.1002/2014JA020506.

Isbell, J., A. J. Dessler, and J. H. Waite Jr. (1984), Magnetospheric energization by interaction between planetary spin and the solar wind, *J. Geophys. Res.*, *89*, 10,716–10,722, doi:10.1029/JA089iA12p10716.

Jia, X., and M. G. Kivelson (2012), Driving Saturn's magnetospheric periodicities from the upper atmosphere/ionosphere: Magnetotail response to dual sources, *J. Geophys. Res.*, *117*, A11219, doi:10.1029/2012JA018183.

Jia, X., M. G. Kivelson, and T. I. Gombosi (2012), Driving Saturn's magnetospheric periodicities from the upper atmosphere/ionosphere, *J. Geophys. Res.*, *117*, A04215, doi:10.1029/2011JA017367.

Jinks, S. L., et al. (2014), Cassini multi-instrument assessment of Saturn's polar cap boundary, *J. Geophys. Res. Space Physics*, *119*, 8161–8177, doi:10.1002/2014JA020367.

Kellett, S., C. S. Arridge, E. J. Bunce, A. J. Coates, S. W. H. Cowley, M. K. Dougherty, A. M. Persoon, N. Sergis, and R. J. Wilson (2011), Saturn's ring current: Local time dependence and temporal variability, *J. Geophys. Res.*, *116*, A05220, doi:10.1029/2010JA016216.

Kurth, W. S., T. F. Averkamp, D. A. Gurnett, J. B. Groene, and A. Lecacheux (2008), An update to a Saturnian longitude system based on kilometric radio emissions, *J. Geophys. Res.*, *113*, A05222, doi:10.1029/2007JA012861.

Lamy, L. (2011), Variability of southern and northern SKR periodicities, in *Planetary Radio Emissions VII*, edited by H. O. Rucker et al., pp. 39–50, Austrian Acad. Sci. Press, Vienna.

Mardia, K. V., and P. E. Jupp (2000), *Directional Statistics*, Wiley, Chichester, U. K.

Markwardt, C. B. (2009), Non-linear least-squares fitting in IDL with MPFIT, *Astron. Data Anal. Software Syst. XVIII ASP Conf. Ser.*, *411*, 251–254.

Meredith, C. J., S. W. H. Cowley, K. C. Hansen, J. D. Nichols, and T. K. Yeoman (2013), Simultaneous conjugate observations of small-scale structures in Saturn's dayside ultraviolet auroras – implications for physical origins, *J. Geophys. Res. Space Physics*, *118*, 2244–2266, doi:10.1002/jgra.50270.

Meredith, C. J., I. I. Alexeev, S. V. Badman, E. S. Belenkaya, S. W. H. Cowley, M. K. Dougherty, V. V. Kalegaev, G. R. Lewis, and J. D. Nichols (2014), Saturn's dayside UV auroras: Evidence for morphological dependence on the direction of the upstream interplanetary magnetic field, *J. Geophys. Res. Space Physics*, *119*, 1994–2008, doi:10.1002/2013JA019598.

Müller, A. L., J. Saur, N. Krupp, E. Roussos, B. H. Mauk, A. M. Rymer, D. G. Mitchell, and S. M. Krimigis (2010), Azimuthal plasma flow in the Kronian magnetosphere, *J. Geophys. Res.*, *115*, A08203, doi:10.1029/2009JA015122.

Pontius, D. H., Jr., and T. W. Hill (2009), Plasma mass loading from the extended neutral gas torus of Enceladus as inferred from the observed plasma corotation lag, *Geophys. Res. Lett.*, *36*, L23103, doi:10.1029/2009GL041030.

Provan, G., D. J. Andrews, C. S. Arridge, S. W. H. Cowley, S. E. Milan, M. K. Dougherty, and D. M. Wright (2009), Polarization and phase of planetary period oscillations on high latitude field lines in Saturn's magnetosphere, *J. Geophys. Res.*, *114*, A02225, doi:10.1029/2008JA013782.

Provan, G., D. J. Andrews, B. Cecconi, S. W. H. Cowley, M. K. Dougherty, L. Lamy, and P. Zarka (2011), Magnetospheric period magnetic field oscillations at Saturn: Equatorial phase 'jitter' produced by superposition of southern- and northern-period oscillations, *J. Geophys. Res.*, *116*, A04225, doi:10.1029/2010JA016213.

Provan, G., D. J. Andrews, C. S. Arridge, A. J. Coates, S. W. H. Cowley, G. Cox, M. K. Dougherty, and C. M. Jackman (2012), Dual periodicities in planetary period magnetic field oscillations in Saturn's tail, *J. Geophys. Res.*, *117*, A01209, doi:10.1029/2011JA017104.

Provan, G., L. Lamy, S. W. H. Cowley, and M. K. Dougherty (2014), Planetary period oscillations in Saturn's magnetosphere: Comparison of magnetic oscillations and SKR modulations in the post-equinox interval, *J. Geophys. Res. Space Physics*, *119*, 7380–7401, doi:10.1002/2014JA020011.

Radioti, A., D. Grodent, J.-C. Gérard, B. Bonfond, J. Gustin, W. Pryor, J. M. Jasinski, and C. S. Arridge (2013), Auroral signatures of multiple magnetopause reconnection at Saturn, *Geophys. Res. Lett.*, *40*, 4498–4502, doi:10.1002/grl.50889.

Rohde, R., R. Muller, R. Jacobsen, S. Perlmutter, A. Rosenfeld, et al. (2013), Berkeley Earth Temperature Averaging Process, *Geoinfor. Geostat An Overview*, *1*, doi:10.4172/2327-4581.1000103.

Southwood, D. J., and S. W. H. Cowley (2014), The origin of Saturn magnetic periodicities: Northern and southern current systems, *J. Geophys. Res. Space Physics*, *119*, 1563–1571, doi:10.1002/2013JA019632.

Southwood, D. J., and M. G. Kivelson (2007), Saturn magnetospheric dynamics: Elucidation of a camshaft model, *J. Geophys. Res.*, *112*, A12222, doi:10.1029/2007JA012254.

Southwood, D. J., and M. G. Kivelson (2009), The source of Saturn's periodic radio emission, *J. Geophys. Res.*, *114*, A09201, doi:10.1029/2008JA013800.

Stallard, T., S. Miller, H. Melin, M. Lystrup, M. Dougherty, and N. Achilleos (2007), Saturn's auroral/polar region H_3^+ infrared emission 1. General morphology and ion velocity structure, *Icarus*, *189*, 1–13.

Stallard, T. S., S. Miller, H. Melin, L. M. Trafton, T. R. Geballe, and R. D. Joseph (2004), Ion winds in Saturn's auroral/polar region, *Icarus*, *167*, 204–211.

Talboys, D. L., C. S. Arridge, E. J. Bunce, A. J. Coates, S. W. H. Cowley, M. K. Dougherty, and K. K. Khurana (2009), Signatures of field-aligned currents in Saturn's nightside magnetosphere, *Geophys. Res. Lett.*, *36*, L19107, doi:10.1029/2009GL039867.

Talboys, D. L., E. J. Bunce, S. W. H. Cowley, C. S. Arridge, A. J. Coates, and M. K. Dougherty (2011), Statistical characteristics of field-aligned currents in Saturn's nightside magnetosphere, *J. Geophys. Res.*, *116*, A04213, doi:10.1029/2009JA016102.

Thomsen, M. F., C. M. Jackman, R. L. Tokar, and R. J. Wilson (2014), Plasma flows in Saturn's nightside magnetosphere, *J. Geophys. Res. Space Physics*, *119*, 4521–4535, doi:10.1002/2014JA019912.

Wilson, R. J., R. L. Tokar, M. G. Henderson, T. W. Hill, M. F. Thomsen, and D. H. Pontius (2008), Cassini plasma spectrometer thermal ion measurements in Saturn's inner magnetosphere, *J. Geophys. Res.*, *113*, A12218, doi:10.1029/2008JA013486.

Wilson, R. J., R. L. Tokar, and M. G. Henderson (2009), Thermal ion flow in Saturn's inner magnetosphere measured by the Cassini plasma spectrometer: A signature of the Enceladus torus?, *Geophys. Res. Lett.*, *36*, L23104, doi:10.1029/2009GL040225.